The Pennsylvania State University

The Graduate School

Department of Materials Science and Engineering

PHASE-FIELD MODELS OFIRON PHOSPHATE AND LITHIUM IRON PHOSPHATE BINARY SYSTEM

A Thesis in

Materials Science and Engineering

by

Wenting Xing

Submitted in Partial Fulfillment

of the Requirements

for the Degree of

Master of Science

August 2012

The thesis of Wenting Xing was reviewed and approved* by the following:

Long-Qing Chen

Professor of Materials Science and Engineering

Thesis Advisor

Venkatraman Gopalan

Professor of Materials Science and Engineering

Sulin Zhang

Associate Professor of Engineering Science and Mechanics and Bioengineering

Joan M. Redwing

Professor of Materials Science and Engineering, Chemical Engineering & Electrical Engineering

Chair, Intercollege Graduate Degree Program in Materials Science and Engineering

*Signatures are on file in the Graduate School

Abstract

This thesis describes the phase-field modeling of $FePO_4$-$LiFePO_4$ binary system. Lithium iron phosphate has played an important role as a cathode material in rechargeable lithium-ion batteries due to its cycle life, safety and stability. The thermodynamics and two-phase morphologies of lithium iron phosphate are studied by combining the phase-field method with microelasticity theory.

The simple regular solution model has been used first to investigate the coherency strain energy contribution to this binary system. We also developed the fitted expression of the existing experimental data on the phase diagram, as well as the effect of coherency strain energy on the phase diagram. It was found that coherency strain energy could significantly suppress the miscibility gap. We predicted the optimum habit planes analytically as well as using three-dimensional phase-field simulations. The results will be compared with experimental observation, which show excellent agreement.

The phase transitions and morphology of microstructure in a nanoparticle in the binary system due to the lithium diffusion process can be observed by combining the smooth boundary method and phase-field model.

Table of Contents

List of Figures

List of Tables

Acknowledgements

For helpful suggestions and unlimited support received during my undergraduate and graduate studies I wish to express my appreciative thanks to my advisor, Professor Long-Qing Chen. Under his guidance, I started to understand not only how to be a researcher, but also a human being. I really enjoyed the time in my group; for me, they are all like my family. I wish to thank my labmates, my “big brothers”, Dr. Linyun Liang, Dr. Liang Hong, Dr. Tae WookHeo, Dr. Benjamin Winchester, Mr. YijiaGu, Mr. Ye Cao, Mr. Jason Britson, Mr. FeiXue, Mr. Chen Duan, Mr. Tiannan Yang, Mr. Jiamian Hu, Mr. YanzhouJi, Mr. Charles Brooks, and many others, for their helpful advice on my research as well as my life.

I would like to thank Dr. VenkatGopalan and Dr. Sulin Zhang for serving on my committees.

I would also like to especially thank to my parents for their love, support, and understanding. They are staying with me, listening to me, and helping me anytime. In the end, I would like to give my special thanks to my grandparents. They started my dream to be a scientist with full support. Their spirit and love will live in my heart and soul forever.

CHAPTER 1

INTRODUCTION

1.1 Introduction

For the better part of the last two centuries, fossil fuels have played an important role in the energy system. What has been made clear is that these forms of energy are harmful to the environment. Burning coal, gas, and oil was by far the best method of generating energy, so it was used everywhere. Most technologies are still dependent on these types of fuel, even though we now know the danger they are. Fossil fuels are burned and release carbon dioxide, which is a greenhouse gas, and pollutes the atmosphere. For this reason the development of cleaner, reusable resources is the most important technological field in the 21st century, and possesses the greatest potential for economic and scientific gain. As an important cleaner and reusable energy resource, Li-ion batteries, which have large working cell voltages, high energy density, light weight and many other advantages [1-6], have been used in many products such as cell phones, laptops, cameras etc. It shows great potential to be developed and used into wider fields. Lithium iron phosphate ($LiFePO_4$) has attracted much attention as an electrode in

rechargeable Li-ion batteries [1] due to its large theoretical capacity of 170 mAh/g [2, 3, 4] and combined with a lithium intercalation potential of 3.5 V [2, 5]. As is shown in Fig. 1.1 [6], Li-ion batteries provide small size with lightweight while maintaining high energy density.

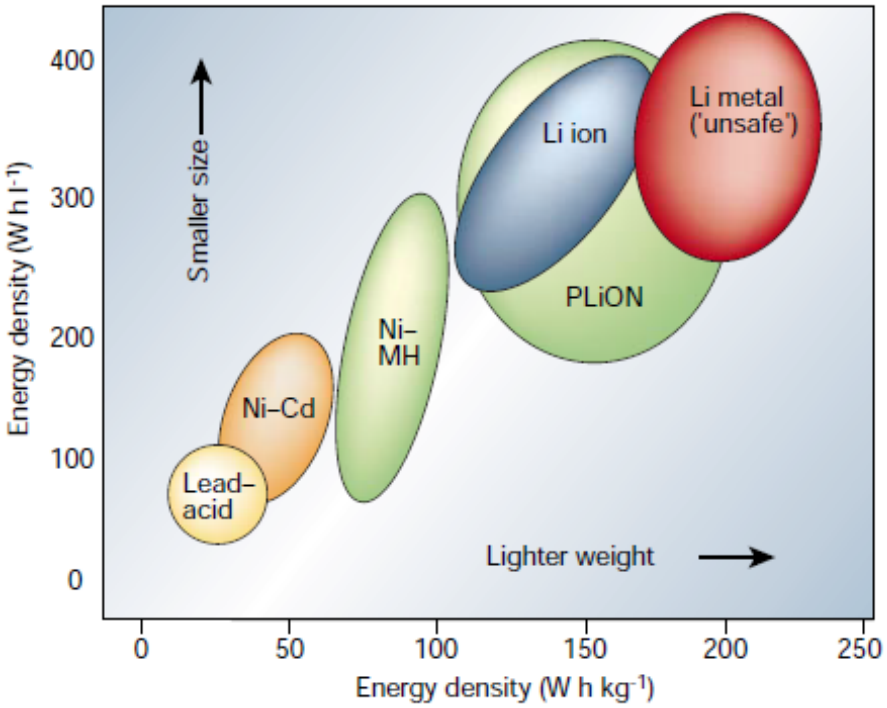

Fig. 1.1 Volumetric vs. gravimetric energy density comparison of the different battery technologies.

Chemical reactions occur through the exchange of atoms and electrons between molecules. In an electrochemical cell, the reactants are physically separated such that electrons can be transferred to do useful work. The study of these reactions, and the

resulting transfer of electrons, is called electrochemistry.The main consideration of any battery technology is the material selections that form the positive and negative electrodes, which are related to the performance (cell potential, capacity, energy density, etc.). The Li-ion battery chemistry can be written as:

Positive Electrode: $LiFePO_4 \rightleftharpoons Li_{1-x}FePO_4 + xLi^+ + xe^-$ (1.1a)

Negative Electrode: $C + xLi^+ + xe^- \rightleftharpoons CLi_x$ (1.1b)

Battery Total: $LiFePO_4 + C \rightleftharpoons Li_{1-x}FePO_4 + CLi_x$ (1.1c)

In this study, the cathode is formed by carbon-coated $LiFePO_4$, which appears in the porous structure as shown in Fig. 1.2.The discharging and charging processes in Li-ion batteries depend on the Li^+ and electron diffusion into or out of the cathode particles. A first-order transition occurs between a Li-rich triphylitephase ($LiFePO_4$) and Li-poor heterosite phase ($FePO_4$) in the Li-ion cathode [8].As illustrated in Fig. 1.2, $LiMPO_4$ has an orthorhombic olivine lattice which means the lattice parameters along different directions are all different. At room temperature, Li has about 1-3% solubility in bulk $FePO_4$ and 3-4% solubility in bulk $LiPO_4$ [9-11].

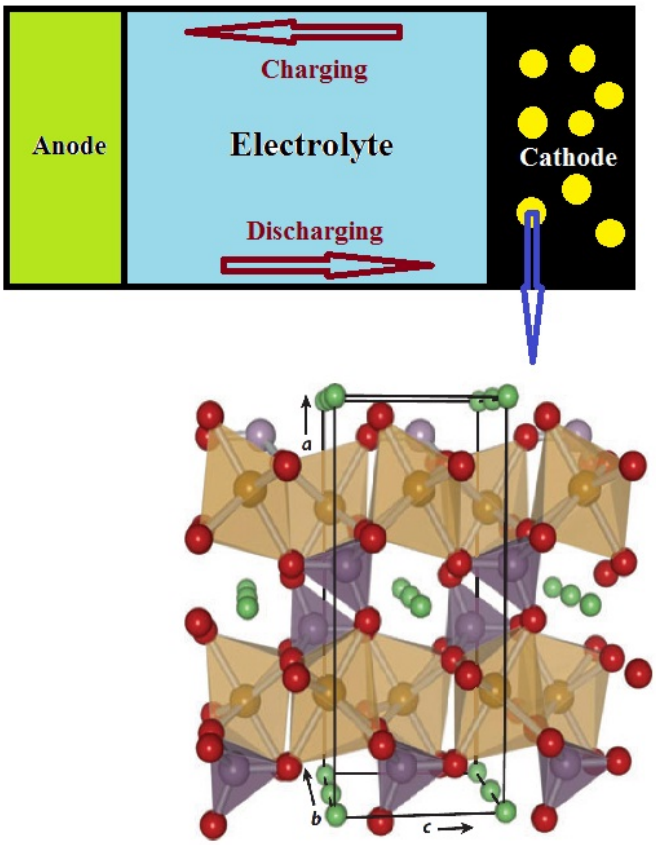

Fig. 1.2 Schematic of Lithium-ion battery (The porous material in the Li-ion battery cathode is $LiFePO_4$ <yellow> which is coated by carbon <black>) and orthorhombic olivine structure of $LiFePO_4$ [7] (where Li atoms are green, PO_4 is purple polyhedral, and FeO_6 is brown polyhedral).

1.2 Research objectives

Materials are designed and controlled to exhibit certain desired properties. These properties are controlled by the underlying microstructure. The atomic structure is not sufficient to analyze these materials; instead the majority of advanced materials require a nanoscale or microscale microstructure, characterized by the number of faces, shapes, sizes, etc. Most desired microstructures and properties are obtained from empirical and semiemperical experimental methods. However, a theoretical prediction of the microstructure can become feasible due to advances in computational resources. In order to observe the phase transformations between $FePO_4$ and $LiFePO_4$, the phase-field model, which has been shown to be a powerful tool for microstructure evolution [12], is used. This method predicts the phase transition due to coherency energy effect, Li diffusion kinetics in a nanoparticle and other effects in a Li-ion battery cathode.

The strong coherency energy contribution drives lithium iron phosphate ($LiFePO_4$) to phase-separate into lithium-rich and lithium poor phases [1, 5, 7, 10, 11, 13]. The habit plane of elastic energy effect has been experimentally observed.

In this thesis, the thermodynamics and two-phase morphologies of lithium iron phosphate are studied by combining the phase-field method with microelasticity theory. The habit planes are predicted analytically by using thermodynamics and microelasticity theory, especially the optimum habit plane is determined. The three-dimensional phase-field simulations show excellent agreement with analytical calculations as well as the existing experimental observations [14, 15].

1.3 Thesis structure

This thesis will consist of six chapters.

Chapter 1 provides the introduction and background of lithium-ion batteries, the research objective and thesis structure.

Chapter 2 consists of the general description of phase-field method.

Chapter 3 details the regular solution model analysis of lithium iron phosphate ($LiFePO_4$), including analytical calculation and three-dimensional phase-field simulations.

Chapter 4, the regular solution model with a concentration dependent interaction parameter (using experimental data) analysis of lithium iron phosphate ($LiFePO_4$), including analytical calculations and three-dimensional phase-field simulations.

Chapter 5, smooth boundary method and phase-field model are applied on the regular solution model of lithium iron phosphate ($LiFePO_4$) for the intercalation process.

Chapter 6 concludes this thesis and the discussions on the future work.

References

[1] A. K. Padhi, K. S. Nanjundaswamy, and J. B. Goodenough, *Journal of The Electrochemical Society* **144**, 1188 (1997).

[2] H. Huang, S. C. Yin, and L. F. Nazar, *Electrochemical and Solid-State Letters* **4**, A170 (2001).

[3] A. Yamada and S. –C. Chung, *Jounal of The Electrochemical Society* **148**, A960 (2001).

[4] V. Srinivasan and J. Newman, *Journal of The Electrochemical Society* **151**, A1517 (2004).

[5] J. L. Dodd, R. Yazami, and B. Fultz, *Electrochemical and Solid-State Letters* **9**, A151-A155(2006).

[6] J. –M. Tarascon and M. Armand, *Nature* **414**, 359 (2001).

[7] T. Maxisch and G. Ceder, *Physical Review B* **73**, 174112 (2006).

[8] M. Tang, C. W. Carter, and Y. –M. Chiang, *Annual Review of Materials Research* **40**, 501-529 (2010).

[9] A. Yamada, H. Koizumi, N.Sonoyama, and R.Kanno, *Electrochemical and Solid-State Letters* **8**, A409-A413 (2005).

[10] C. Delacourt, P.Poizot, J. –M.Tarascon, and C.Masquelier, *Nature Materials* **4**, 254-260 (2005).

[11] N. Meethong, H. –Y. S. Huang, C. W. Carter, and Y. –M. Chiang, *Electrochemical and Solid-State Letters* **10**, A134-A138 (2007).

[12] L. –Q. Chen, *Annual Review of Materials Research* **32**, 113-140(2002).

[13] A. Yamada, H. Koizumi, S. –I. Nishimura, N. Sonoyama, R. Kanno, M. Yonemura, T. Nakamura, and Y. Kobayashi, *Nature Materials* **5**, 357-360 (2006).

[14] G. Chen, X. Song, and T. J. Richardson, *Electrochemical and Solid-State Letters* **10**, A134-A138 (2007).

[15] C. V. Ramana, Z. Mauger, F. Gendron, C. M. Julien, and K. Zaghib, *Journal of Power Sources* **187**, 555-564 (2009).

CHAPTER 2

PHASE-FIELD METHODS

2.1 Introduction

Underlying microstructures play a significant role in materials science and engineering since it is directly related with the properties of most engineered materials. The process of solidification, solid-state precipitation, and thermomechanical processing, which is used to advance microstructures, is controlled by free boundary dynamics and nonequilibrium phase transformation kinetics.

The phase-field method is the best available tool to determine the complicated microstructure evolution [1]. This method uses thermodynamic data to understand the kinetics of microstructure evolution and has become one of the most important parts of computational materials science. Phase-field approach can be used to describe multiple problems, such as nucleation and spinodal decomposition, grain growth, first and second-order phase transitions, coarsening, order-disorder transitions, solidification, crystal growth, diffusion controlled processes, solute drag, effects of anisotropy, and interdiffusion [1].

Phase-field was introduced in the late 1970s and reported in the 1980s. It showed a great potential in solving phase transition problems. In order to solve two problems, surface tension and super cooling, not captured in classical Stefen problems, this method had been improved by Fix in 1983 [2]. Phase variable, so-called order parameter, is determined by field equation and solid-liquid interface. A published “thermodynamically-consistent” phase-field model was published by Penrose and Fife in 1990. Instead of using the Landau–Ginzbug free energy functional, they used the analogous entropy functional [3]. The phase-field method is greatly suited for modeling the complex morphologies in the microstructure studies.

2.2 Order parameters

The states of a system of phase transformations are usually studied from basic thermodynamics, which is generally described by bulk variables including pressure, volume, average density, and internal energy. The order parameter is a part of a free energy functional, which is defined for the system. A variational method can be used to determine evolution equations to find the system, which contains the minimum of the energy functional. Two types of field variables, conserved and nonconserved, are used in the diffusion-interface issue of the phase-field model. The total free energy of the inhomogeneous microstructure systems is written as [4]

$$F = \int \left[f(c_1, c_2, \ldots, c_n, \eta_1, \eta_2, \ldots, \eta_p) + \sum_{i=1}^{n} \alpha_i (\nabla c_i)^2 + \sum_{i=1}^{3} \sum_{j=1}^{3} \sum_{k=1}^{p} \beta_{ij} \nabla_i \eta_k \nabla_j \eta_k \right] d^3 r$$

$$+ \iint G(r - r')\, d^3 r d^3 r', \qquad (2.1)$$

wherec_1, c_2, …, c_n are conserved variables, η_1, η_2, …, η_p are nonconserved variables, f is the local free energy, α_i and β_{ij} are the gradient energy coefficients. This function includes both short-range and long-range terms that contribute to free energy. The first integral term indicates the short-range chemical interactions, which is the local energy contribution; and the second integral term describes long-range interactions that include elastic interactions, magnetic field interactions, electrostatic interactions and so on, are nonlocal free energy contribution. Choosing order parameter variables is one way to distinguish different phase-field models.

2.3 The Landau theory of phase transformation

The order parameter has been treated as a state variable, which can be used to determine ordered and disordered phases in Landau theory of phase transformations. It can be easily defined that the disordered state is $\phi = 0$, while ordered state is $\phi \neq 0$.

Landau introduces a concept of broken symmetry into the phase transformation theory, and also relates it with order parameter. Broken symmetry means a certain number of symmetries give rise to phases that showthe same amount of symmetries

above the temperature where fewer symmetries are displayed below it [5]. If we write the atomic distribution function in crystal above the phase transformation temperatureas $\rho_0(r)$, this function will keep constant under any symmetric operation in space group Γ_0. However, if the state of crystal slightly changed with decreasing temperature, it exhibits less symmetry in the crystal; the density function can change to

$$\rho(r) = \rho_0(r) + \delta\rho(r), \tag{2.2}$$

where the symmetry group of ρ is Γ, andΓ is the subgroup of Γ_0.

Any given functionρ can be expressed as a linear combination of variables, like $\varphi_1, \varphi_2, \ldots, \varphi_n$; and these variables can transform into each other under the symmetry operation in group Γ. These transformation matrices form the basis function,$\varphi_1, \varphi_2, \ldots, \varphi_n$, for theexpression of symmetry group Γ. The choice of the variables $\varphi_i(i = 1,2,\ldots)$ is not unique, but it can be always expressed in this way: separate them into several groups, each group containingthe least possible number of variables; these variables can transform with each other. Each group in the transformation matrices form the irreducible representation of the symmetry groupΓ.

Then we write $\delta\rho$as a function of the variables $\varphi_i^{(n)}$, which is the irreducible representation basis function of group Γ_0 [6].

$$\delta\rho = \sum_n \sum_i \eta_i^{(n)} \varphi_i^{(n)}, \tag{2.3}$$

where $\eta_i^{(n)}$ is a scalar coefficient, the first summation term is for the irreducible representations, and second summation term is for each variable.

We can think that $\delta\rho$ corresponds to a single irreducible representation in the group Γ_0 under continuous phase transformations, because there are almost no two separate irreducible representations that transform at the same temperature. The equation above can be expressed as

$$\delta\rho(r) = \sum_i \eta_i \varphi_i(r). \tag{2.4}$$

And every basis function of the space group is given by

$$\varphi_i(r) = u_{i,q}(r)\exp(iq \cdot r), \tag{2.5}$$

where $u_{i,q}(r)$ is the periodic characteristic of crystal lattice,and q is reciprocal lattice to describe the irreducible representations.

When the temperature is at the phase transition temperature, $T = T_c$, η_i has to be zero based on symmetry, which means,

$$\delta\rho = 0,\ \rho = \rho_0 \tag{2.6}$$

where$\eta_i = \eta r_i$ and $\sum_i r_i^2 = 1$, thus,

$$\eta^2 = \sum_i \eta_i^2. \tag{2.7}$$

Since we consider the continuous phase transition, the coefficients η_i approximate to zero when the temperature nears the phase transition point. Therefore the total free energy can be expressed as a polynomial function of η_i,

$$G = G_0 + a\eta f^{(1)} + A\eta^2 f^{(2)} + b\eta^3 f^{(3)} + B\eta^4 f^{(4)} + \cdots, \tag{2.8}$$

coefficient a, A, b, B, … usually are functions of temperature, and *f* is linear inequality of r_i. And $f^{(1)} = 0$, because there is no phase transformation, and second order exists, $f^{(2)} = 1$. So the equation can be rewritten as

$$G = G_0 + A\eta^2 f^{(2)} + b\eta^3 f^{(3)} + B\eta^4 f^{(4)} + \cdots. \tag{2.9}$$

2.4 Evolution equations

The spatial and temporal distributions of the order parameters (the field variables, which change continuously from one phase to another) in a phase-field model is formed by solving the Cahn-Hilliard nonlinear diffusion equation [7] and the time-dependent Ginzburg-Landau Allen-Cahn [8] equation,

$$\frac{\partial c(r,t)}{\partial t} = M\nabla^2 \frac{\delta F}{\delta c(r,t)} \tag{2.10}$$

$$\frac{\partial \eta_p(r,t)}{\partial t} = -L_{pq} \frac{\delta F}{\delta \eta_q(r,t)} \tag{2.11}$$

where$M_{ij}$is kinetic coefficient that is related to $c_1,\ c_2,\ \ldots,\ c_n$ for conserved system and $L_{pq}$is kinetic coefficient that is related to $\eta_1,\ \eta_2,\ \ldots,\ \eta_p$ for nonconserved system, and F is the total free energy of the system.

These two equations are nonlinear, so they can only be solved numerically through discretization in space and time. Since the explicit schemes cause severe time step restrictions and do not satisfy a discrete energy law, semi-implicit and fully implicit schemes are good to use. The semi-implicit method isan efficient and accurate numerical method to solve the Cahn-Hilliard and Allen-Cahn equations with larger time step sizes [9, 10]. This new algorithm can be applied with different types of boundary conditions using spectral methods. The difficulty is in cases without smooth interfaces; the standard

uniform grid is incapable of resolving the solution without using a large amount of grid points.

2.5 Applications

Phase-field can be used to describe many different materials problems; however, there are three major applications: solidification, solid-state phase transformations [11-14], and grain growth [15-17] and coarsening [18-20]. Solidification is a phase transformation in which liquid phase changes to a solid phase when the temperature is below the equilibrium melting temperature (freezing point). Solid-state phase transformations simply mean phase transformation occurs in the solid-state, where phase-field is always used to deal with the diffusional and diffusionless issues. Grain growth is the process where a material's grain boundaries increase in size at elevated temperatures. Many phase-field applications are summarized in Table 2.1 [4].

Table 2.1 Applications of the phase-field method

<table>
<tr><th>Solidification</th><th>Solid-State Phase Transformations</th><th>Coarsening and Grain Growth</th><th>Other Applications</th></tr>
<tr><td>Pure liquid</td><td>Spinodal phase separation</td><td rowspan="2">Coarsening</td><td>Phase transformations in thin films</td></tr>
<tr><td>Pure liquid with fluid flow</td><td>Precipitation of cubic ordered intermetallic</td><td>Surface-stress induced pattern formation</td></tr>
<tr><td rowspan="2">Binary alloys</td><td>Precipitates from a disordered matrix</td><td rowspan="2">Grain growth in a single-phase solid</td><td>Spiral growth</td></tr>
<tr><td>Cubic-tetragonal transformations</td><td>Crystal growth under stress</td></tr>
<tr><td rowspan="2">Multicomponent alloys</td><td>Hexagonal to orthorhombic transformations</td><td rowspan="2">Grain growth in a two-phase solid</td><td>Solute-dislocation interactions</td></tr>
<tr><td>Ferroelectric transformations</td><td>Dislocation dynamics</td></tr>
<tr><td rowspan="2">Nonisothermal solidification</td><td>Phase transformations under an applied stress</td><td rowspan="2">Anisotropic grain growth</td><td>Crack propagation</td></tr>
<tr><td>Martensitic transformations in single and polycrystals</td><td>Electromigration</td></tr>
</table>

References

[1] I. Singer-Loginova and H. M. Singer, *Reports on Progress in Physics* **71**, 32 (2008).

[2] G. Fix, *Free Boundary Problems, Theory and Application*, Pitman, New York, 580-589 (1983).

[3] O. Penrose and P. Fife, *Physica D* **43**, 44-62 (1990).

[4] L. –Q. Chen, *Annual Reviews* **32**, 113-140 (2002).

[5] N.Provatas and K. Elder, *Phase-Field Methods in Materials Science and Engineering*, WILEY-VCH, 17-22 (2010).

[6] J. –C.Tolédano and P.Tolédano, *The Landau Theory of Phase Transitions*, World Scientific, 25-41 (1987).

[7] J. W.Cahn, *Acta Metallurgica* **9**, 795-801 (1961).

[8] S. M. Allen and J. W. Cahn, *Journal de Physique* **38**, C7-51 (1977).

[9] L. –Q. Chen and J. Shen, *Computer Physics Communications* **108**, 147-158 (1998).

[10] J. –Z. Zhu, L. –Q. Chen, J. Shen, and V. Tikare, *Physical Review E* **60**, 3564-3572 (1999).

[11] H. Nishimori and A. Onuki, *Physical Review B* **42**, 980 (1990).

[12] A. Onuki and H. Nishimori, *Physical Review B* **43**, 13649 (1991).

[13] C. Sagui, A. M. Somoza, and R. Desai, *Physical Review E* **50**, 4865 (1994).

[14] Y. Wang, L. –Q. Chen, and A. G. Khachaturyan, *Acta Metallurgicaet Materialia* **41**, 279 (1993).

[15] L. –Q. Chen and Y. H. Wen, *Physical Review B* **50**, 15752 (1994).

[16] D. N. Fan and L. –Q. Chen, *Acta Materialia* **45**, 611 (1997).

[17] C. E. Krill and L. –Q. Chen, *Acta Materialia* **50**, 3057 (2002).

[18] Y. Wang, D. Banerjee, C. C. Su, and A. G. Khachaturyan, *Acta Materialia* **50**, 3057 (2002).

[19] D. Y. Li and L. –Q. Chen, *Acta Materialia* **47**, 247 (1998).

[20] V. Vaithyanathan and L. –Q. Chen, *Scripta Materialia* **42**, 967 (2000).

CHAPTER 3

REGULAR SOLUTION MODEL OF LITHIUM IRON PHOSPHATE ($LiFePO_4$) AND EFFECT OF COHERENT STRAIN ENERGY

3.1 Introduction

Lithium-ion batteries are the current leader for rechargeable, portable energy. They show great potential to be developed and used into wider fields. Lithium iron phosphate, $LiFePO_4$, has always been selected to be the cathode material for rechargeable Lithium-ion batteries because of its anisotropic diffusivity and elasticity [1-3].

The coherency strain energy contribution is considered to show the habit plane formed by lithium-rich and lithium-poor phases, which is due to the difference in the lattice parameters between $FePO_4$-$LiFePO_4$ binary systems, eventhough $FePO_4$ and $LiFePO_4$have the same crystal structures. The experimental phase boundary data of the $FePO_4$-$LiFePO_4$ binary system by Delacourt et al. [4] and Dodd et al. [5] and theoretically calculated phase diagram by Zhou et al. [6] show the two-phase region at

room temperature. The TEM observations of the domains in $Li_{0.5}FePO_4$ by Chen et. al [7] show the alignment in the *bc* plane. In this study, we aim to propose that coherency strain energy contributions show significant effects in terms of the phase diagram and optimum habit plane, which is consistent with experimental results.

3.2 Regular solution model and microelasticity theory

During charging, the lithium ions travel from the cathode to the anode, which is the extraction process of $LiFePO_4$ particles. Likewise, lithium ions travel from anode to cathode during discharging. The $LiFePO_4$ particles are coated in carbon, which will offerelectrons to react with lithium ions to become lithium and are then driven into $FePO_4$to form $LiFePO_4$. This intercalation process will cause a lithium-rich phase and a lithium poor phase based on the lithium concentration in iron phosphate.The formed $LiFePO_4$ has an orthorhombic olivine structure with space group Pnma. The crystal structure of $LiFePO_4$consists of alternating layers of lithium and iron that are separated by a layer of phosphate [8]. When lithium moves into an iron phosphate particle, it is stored in the lithium layer without changing the olivine topology but causes the structure to change from iron phosphate to lithium iron phosphate.This results in transformation strains in the material, which is denoted by ε_{ij} . The transformation strainsare determined by the difference in experimental lattice parameters between two structures. This is calculated using experimental data of lattice parameters from Chen et al. [7], which can be written in matrix form as

$$\varepsilon_{ij} = \begin{pmatrix} 0.0592 & 0 & 0 \\ 0 & 0.0451 & 0 \\ 0 & 0 & -0.0128 \end{pmatrix} \quad (3.1).$$

The elastic constants are determined using first principle GGA+U calculations, which is shown in the matrix (3.2) [8].

$$C_{ijkl} = \begin{pmatrix} 138.9 & 72.8 & 52.5 & 0 & 0 & 0 \\ 72.8 & 198 & 45.8 & 0 & 0 & 0 \\ 52.5 & 45.8 & 173 & 0 & 0 & 0 \\ 0 & 0 & 0 & 36.8 & 0 & 0 \\ 0 & 0 & 0 & 0 & 50.6 & 0 \\ 0 & 0 & 0 & 0 & 0 & 47.6 \end{pmatrix} \text{[GPa]} \quad (3.2)$$

The coherency free energy is defined as the sum of the incoherent free energy and the elastic free energy, with the incoherent free energy collected from literature, which is calculated by first principle calculations for a two-phase model [9].

$$F(c,T) = N_v\left[\Omega c(1-c) + kT\left(c\ln c + (1-c)\ln(1-c)\right)\right] \quad (3.3)$$

where $N_v = 8.396 \times 10^{28} \left[/ m^3 \right]$ [9] and Ω is related to the nearest-neighbor interaction strength between lithium ions, which is equal to $59meV$ [9]. The incoherent free energy shows a two-phase region in the 0.2-0.8 concentration range at room temperature, as illustrated in Fig. 3.1 (a); and complete solid solution at 520K in Fig. 3.1 (b). Fig. 3.1 (c) is combined free energy at 298K and 520K. This equation can be used to calculate the phase diagram of incoherent free energy (Fig. 3.2), which shows the two-phase region has been obtained at room temperature.

The most important part that we wish to determine in this research is the effect of coherency strain energy. Calculating the coherency strain requires use of Khachaturyan's equations of microelasticity theory [10, 11]. For an orthorhombic system, $\Omega_{ij}\left(\vec{n}\right)$ is shown in Eq. 3.5, which is the inverse tensor to (3.4) [10, 11].

$$\Omega_{ij}^{-1}\left(\vec{n}\right) = c_{iklj}\vec{n}_k\vec{n}_l \tag{3.4}$$

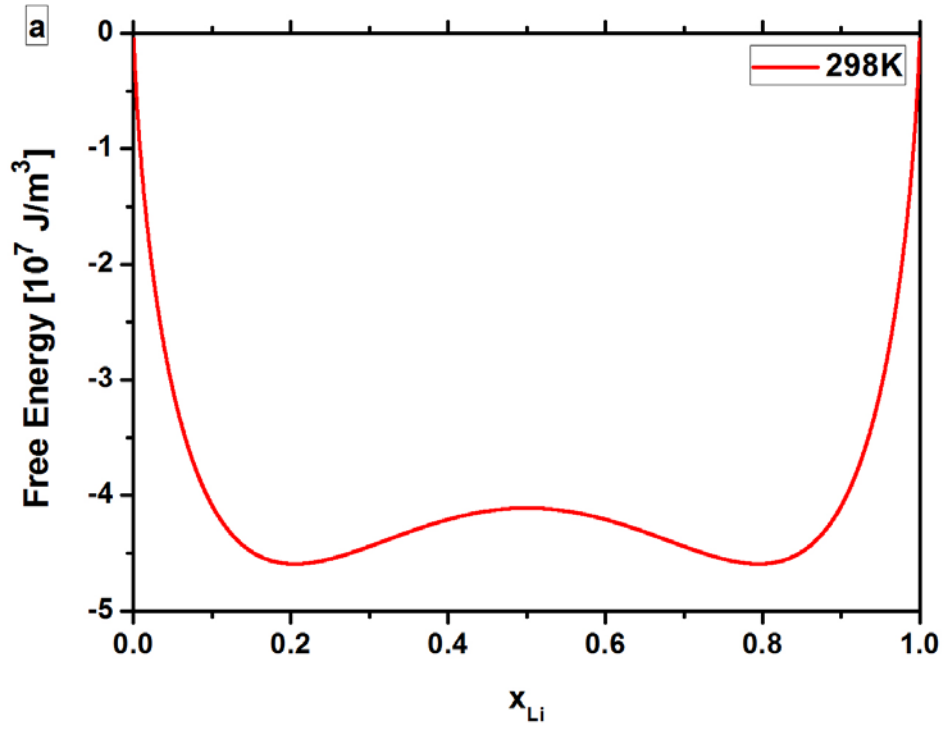
a
298K
Free Energy [10^7 J/m^3]
0
-1
-2
-3
-4
-5
0.0
0.2
0.4
0.6
0.8
1.0
x_Li

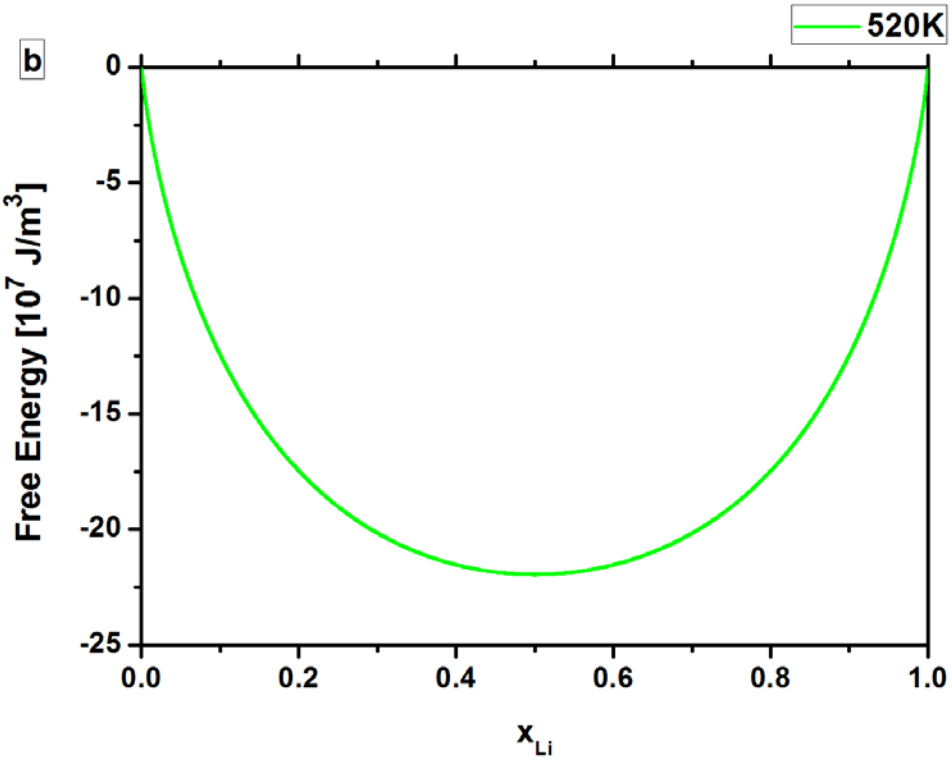
b
520K
Free Energy [10^7 J/m^3]
0
-5
-10
-15
-20
-25
0.0
0.2
0.4
0.6
0.8
1.0
x_Li

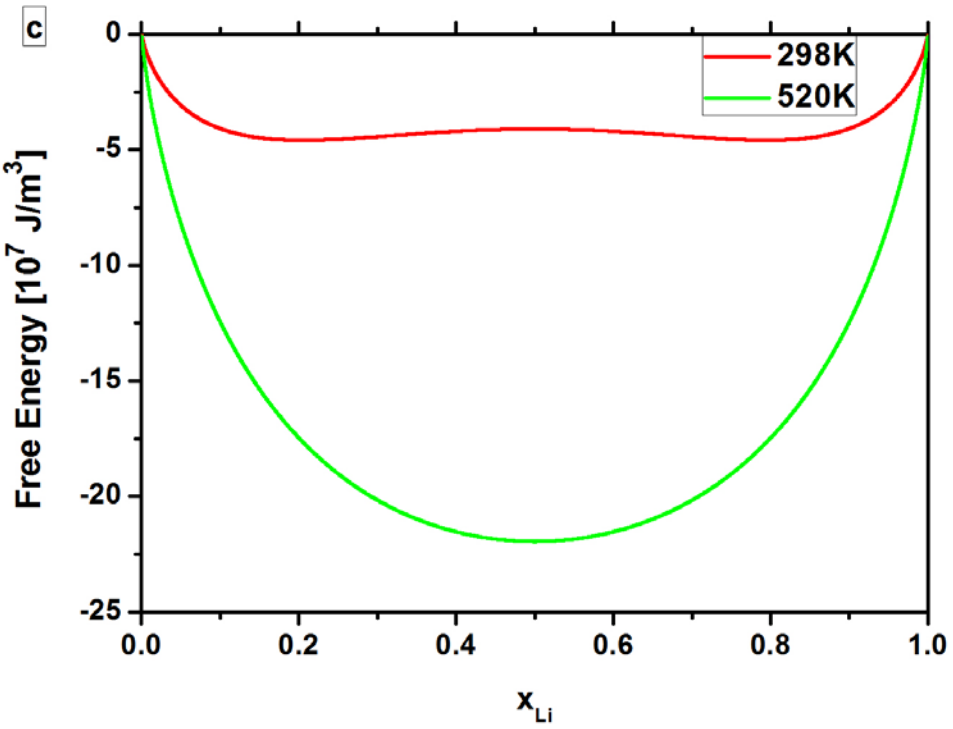

Fig. 3.1 (a) Free energy for regular solution model at room temperature. (b) Free energy for regular solution at 520K. (c) Free energy at 298K and 520K shown on the same plot.

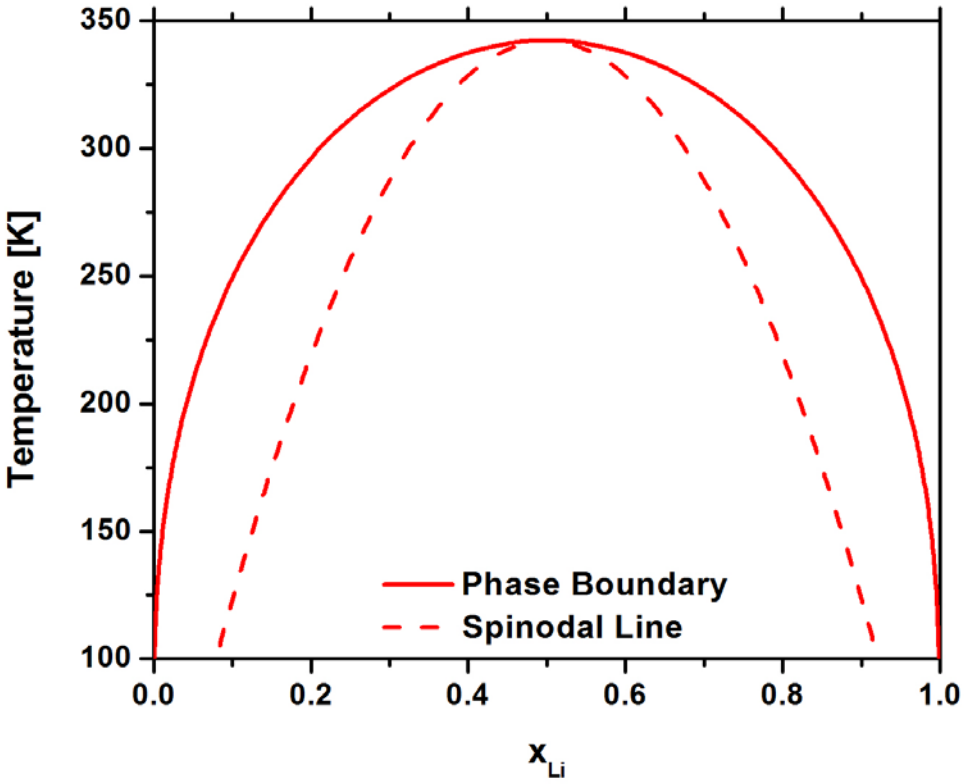

Fig. 3.2 Phase diagram of incoherent free energy for regular solution model.

$$\Omega_{11} = \frac{\alpha\left(c_{55}\vec{n}_1^2 + c_{44}\vec{n}_2^2 + c_{33}\vec{n}_3^2\right) - \beta^2\vec{n}_2^2\vec{n}_3^2}{A\left(\vec{n}\right)}$$

$$\Omega_{12} = \Omega_{21} = \frac{\vec{n}_1\vec{n}_2\left[\beta\gamma\vec{n}_3^2 - \zeta\left(c_{55}\vec{n}_1^2 + c_{44}\vec{n}_2^2 + c_{33}\vec{n}_3^2\right)\right]}{A\left(\vec{n}\right)}$$

$$\Omega_{13} = \Omega_{31} = \frac{\vec{n}_1\vec{n}_3\left(\beta\zeta\vec{n}_2^2 - \alpha\gamma\right)}{A\left(\vec{n}\right)}$$

$$\Omega_{22} = \frac{\eta\left(c_{55}\vec{n}_1^2 + c_{44}\vec{n}_2^2 + c_{33}\vec{n}_3^2\right) - \gamma^2\vec{n}_1^2\vec{n}_3^2}{A\left(\vec{n}\right)}$$

$$\Omega_{23} = \Omega_{32} = \frac{\vec{n}_2\vec{n}_3\left(\gamma\zeta\vec{n}_1^2 - \beta\eta\right)}{A\left(\vec{n}\right)}$$

$$\Omega_{33} = \frac{\alpha\eta - \zeta^2\vec{n}_1^2\vec{n}_2^2}{A\left(\vec{n}\right)} \tag{3.5}$$

where the variables can be defined as

$$\begin{aligned} A\left(\vec{n}\right) = {} & \gamma\vec{n}_1^2\vec{n}_3^2\left[\beta\zeta\vec{n}_2^2 - \alpha\gamma\right] - \beta\vec{n}_2^2\vec{n}_3^2\left[-\gamma\zeta\vec{n}_1^2 + \beta\eta\right] \\ & + \alpha\left[-\zeta^2\vec{n}_1^2\vec{n}_2^2 + \left(c_{55}\vec{n}_1^2 + c_{44}\vec{n}_2^2 + c_{33}\vec{n}_3^2\right)\eta\right] \end{aligned} \tag{3.6}$$

and

$$\begin{aligned} \alpha &= c_{66}\vec{n}_1^2 + c_{22}\vec{n}_2^2 + c_{44}\vec{n}_3^2 \\ \beta &= c_{44} + c_{23} \\ \gamma &= c_{55} + c_{13} \\ \zeta &= c_{66} + c_{12} \\ \eta &= c_{11}\vec{n}_1^2 + c_{66}\vec{n}_2^2 + c_{55}\vec{n}_3^2 \end{aligned} \tag{3.7}$$

The anisotropic elastic can be calculated as a function of direction (3.8) [10-11].

$$B(\vec{n}) = c_{ijkl}\varepsilon_{ij}\varepsilon_{kl} - L(\vec{n}) \tag{3.8}$$

$$L(n) = \vec{n}_i \sigma_{ij} \Omega_{jk}\left(\vec{n}\right)\sigma_{kl}\vec{n}_l \tag{3.9}$$

$$\sigma_{ij} = c_{ijkl}\varepsilon_{kl} \tag{3.10}$$

The average coherency energy contribution is calculated using [10-11]

$$\left\langle L\left(\vec{n}\right)\right\rangle = \frac{1}{4\pi}\int_0^{\pi}\int_0^{2\pi} L\left(\vec{n}\right)\sin\theta d\varphi d\theta \tag{3.11}$$

$\vec{n}$ is the interface normal, the minimum of $B(\vec{n})$ shows the optimum habit plane direction, which is the preferred orientation of the phase boundary with minimized elastic energy contribution. The coherent free energy of the experimental observed habit plane (100) and calculated optimum habit plane (0.832, 0, 0.555) is illustrated in Fig. 3.3. All five different orientations have been calculated and shown on the phase diagram in Fig. 3.4. The phase diagram curve shifts down when different orientations of heterogeneous elastic energy are added. This shows the possibility of seeing a solid solution or single phase region around room temperature, which can help us to understand why the solid solution phases exist at room temperature as shown by Yamada et al. [12]. Also it shows very close phase diagram curves between optimum habit plane and habit plane (100).

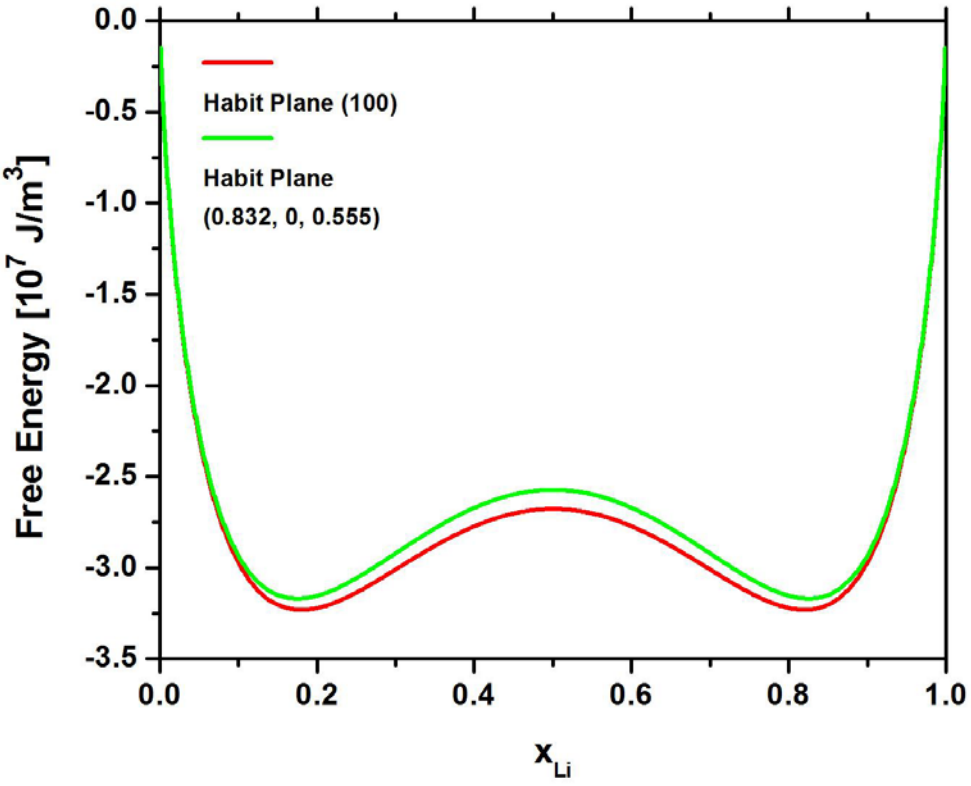

Fig. 3.3 Coherent strain energy considered free energy for regular solution model at 229K.

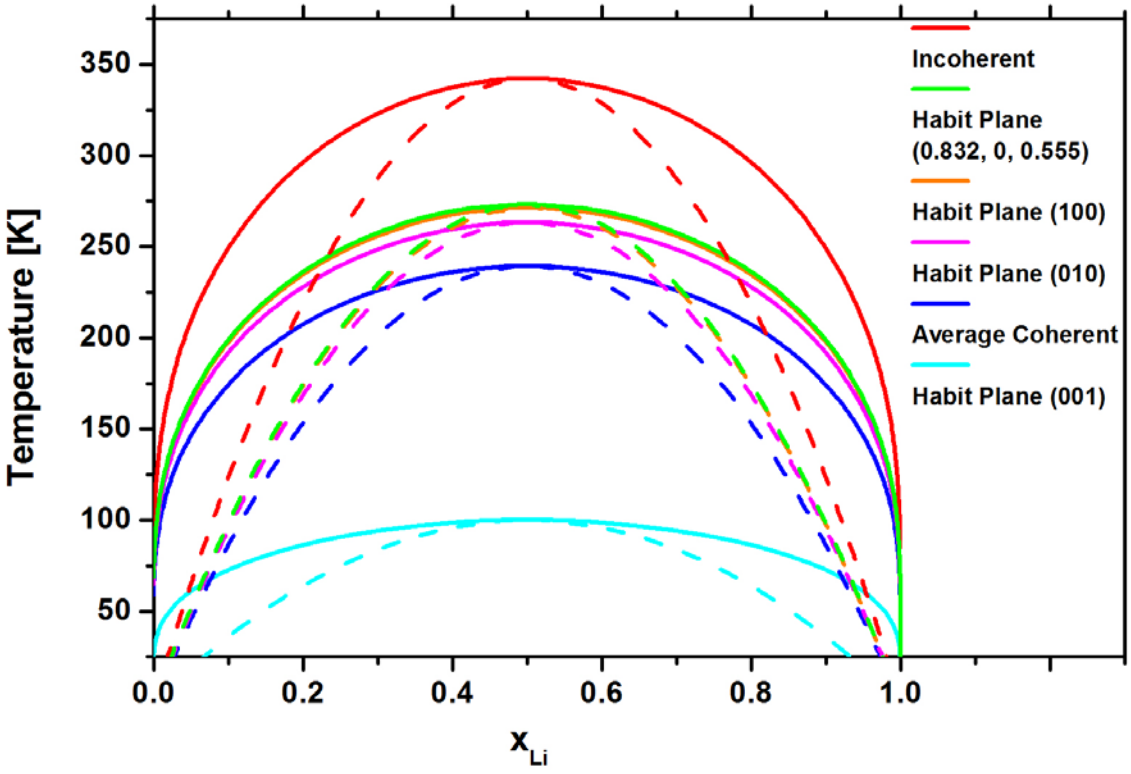

Fig. 3.4Phase boundaries (solid lines) and spinodal lines (dashed lines) of $FePO_4$-$LiFePO_4$ binary system for different habit planes.

3.3 Phase-field model

In order to build the temporal evolution of lithium concentration in a nanoparticle, we choose the lithium concentration as the order parameter. The evolution of lithium concentration is determined by the Cahn-Hilliard diffusion equation by,

$$\frac{\partial c_{Li}(r,t)}{\partial t} = \nabla \cdot \left[M \nabla \frac{\delta F}{\delta c_{Li}} \right] \tag{3.12}$$

where c_{Li} is the concentration of lithium, t is time, M is mobility, and F is the total free energy which can be written as

$$F = \int \left[f_{chemical} + \kappa^2 \nabla^2 c_{Li} + f_{elastic} \right] dV \tag{3.13}$$

where $f_{chemical}$ is the chemical energy density (incoherent free energy density), κ is a gradient coefficient, and $f_{elastic}$ is the elastic energy density.

3.4 Simulation results and discussion

In thephase-field simulations, we employ $64\times64\times64$ three dimensional discrete grid points, and periodic boundary conditions along all the directions. The grid space is chosen to be $dx = dy = dz = 1.0$. The time step for integration is $dt = 0.05$. The gradient coefficient is $\kappa = 0.25$ and initial concentration is $c_0 = 0.5$. As expected, the strong anisotropic elasticity with clear habit plane is shown in the simulation results (Fig. 3.5) at 229K due to spinodal decomposition.

Fig. 3.6 exhibits the two dimensional x-z cross sectional face and x-y cross sectional face to determine habit plane.

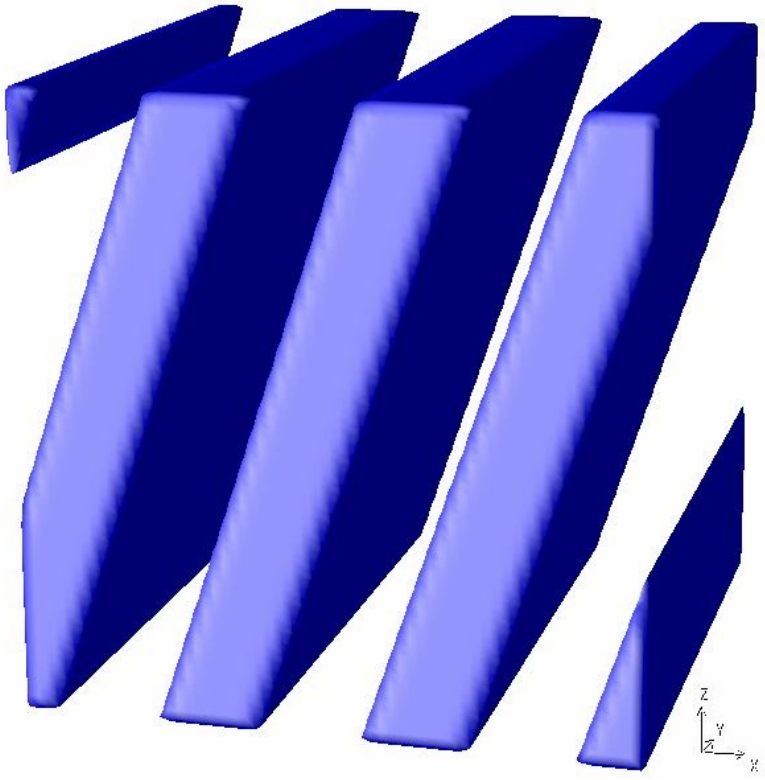

Fig. 3.5Three dimensional morphology of regular solution model of $FePO_4$-$LiFePO_4$ binary system at 229K.

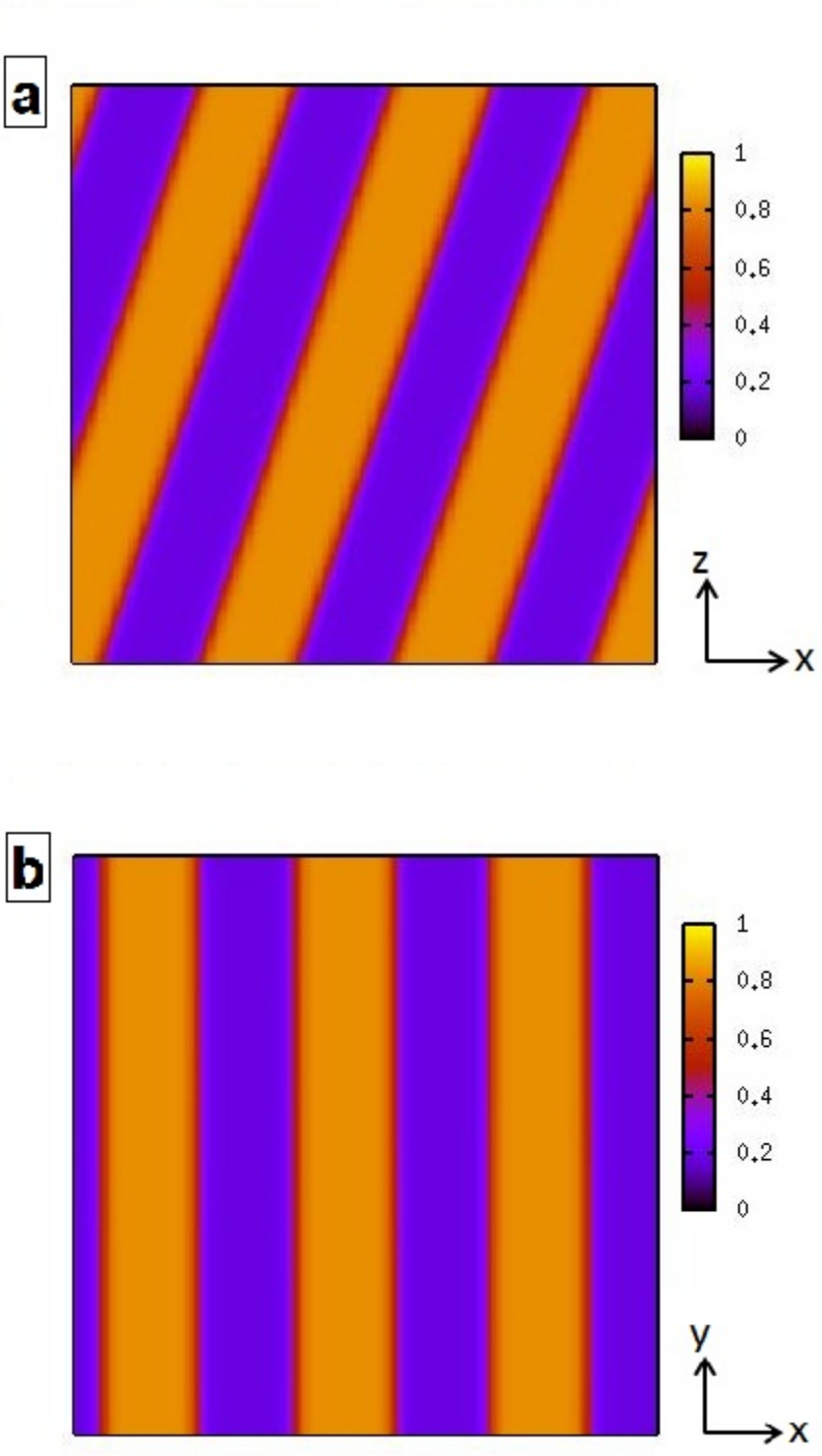

Fig. 3.6 (a) x-z cross sectional face and (b) x-y cross sectional face of three dimensional morphology of regular solution model of $FePO_4$-$LiFePO_4$ binary system at 229K.

As Fig. 3.6 (b) shows, the habit plane is along the y direction which is consistent to our calculation. The determined habit plane needs to be converted into an orthorhombic system (3.14) by using the experimental lattice parameters [7] since the periodic boundary conditions along all the directions in the simulation.

$$
\begin{aligned}
n_1^o &= \frac{n_1 / a}{\sqrt{\left(n_1 / a\right)^2 + \left(n_2 / b\right)^2 + \left(n_3 / c\right)^2}} \\
n_2^o &= \frac{n_2 / b}{\sqrt{\left(n_1 / a\right)^2 + \left(n_2 / b\right)^2 + \left(n_3 / c\right)^2}} \\
n_3^o &= \frac{n_3 / c}{\sqrt{\left(n_1 / a\right)^2 + \left(n_2 / b\right)^2 + \left(n_3 / c\right)^2}}
\end{aligned}
\qquad (3.14)
$$

The determined habit plane is (0.794, 0, 0.608) after conversion, which has 4.78% difference in x direction and 8.72% difference in z direction compared with calculated habit plane (0.832, 0, 0.555). The optimum habit plane is preferred from free energy, phase diagram and simulations, however (100) has been observed in some experiments (Fig. 3.7) [7]. The possible reason for this observation is due to defects which could partially lose coherency energy to show the minimum total energy, where the experimental literature [7] also reported the cracks and dislocations observation. It could also be due to the anisotropic interfacial energy, where (100) may show lower interfacial energy than the optimum habit plane which gives the lowest total energy contribution.

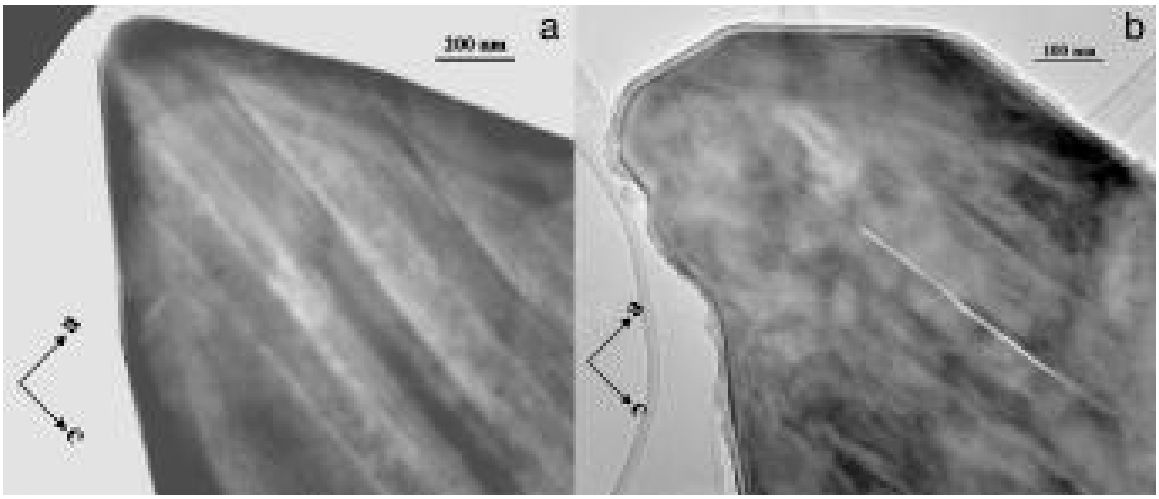

Fig. 3.7 Transmission electron microscopy image showing the domains in $Li_{0.5}FePO_4$ crystal. The phase boundary is parallel to *bc* plane, (100) plane.

3.5 Summary

In summary, the thermodynamics and two-phase morphologies of lithium iron phosphate are studied by combining the phase-field method with microelasticity theory. The calculated phase diagram and three dimensional phase-field simulations show a consistent optimum habit plane, which has a really close total free energy to the experimentally observed habit plane (100).

References

[1] D. Morgan, A. Van der Ven, and G. Ceder,*Electrochemical and Solid-State Letters* **7**, A30-A32 (2004).

[2] M. S. Islam, D. J. Driscoll, C. A. J. Fisher, and P.R. Slater, *Chemistry of Materials* **17**, 5085-5092(2005).

[3] T. Maxisch and G. Ceder, *Physical Review B* **73**, 174112 (2006).

[4] C. Delacourt, P. Poizot, J. –M. Tarascon, and C. Masquelier, *Nature Materials* **4**, 254-260 (2005).

[5] J. L. Dodd, R. Yazami, and B. Fultz, *Electrochemical and Solid-State Letters* **9**, A151-A155 (2006).

[6] F. Zhou, T. Maxisch, and G. Ceder, *Physical Review Letters* **97**, 155704 (2006).

[7]G. Chen, X. Song, and T. J. Richardson, *Electrochemical and Solid-State Letters* **9**, A296 (2006).

[8] T. Maxisch, and G. Ceder, *Physical Review B* **73**, 174112 (2006).

[9] B. C. Han, A. Van der Ven, D. Morgan, and G. Ceder, *Electrochimica Acta* **49**, 4694-4695 (2004).

[10] A. G. Khachaturyan, *Theory of Structural Transformations in Solids* (Dover Publications, 2008).

[11]A. G. Khachaturyan, *Soviet Physics – Solid State* **8**, 2163-2168 (1967).

[12] A. Yamada, H. Koizumi, N. Sonoyama, and R. Kanno, *Electrochemical and Solid-State Letters* **8**, A409 (2005).

CHAPTER 4

REGULAR SOLUTION MODEL WITH CONCENTRATION DEPENDENT INTERACTION PARAMETER OF LITHIUM IRON PHOSPHATE ($LiFePO_4$) AND EFFECT OF COHERENT STRAIN ENERGY

4.1 Introduction

As we mentioned in chapter 3, the experimental phase boundary data of the $FePO_4$-$LiFePO_4$ binary system by Delacourt et al. [1] and Dodd et al. [2] and theoretically calculated phase diagram by Zhou et al. [3] are showing similar “middle compressed” phase diagram (Fig. 4.1) [3]. In the regular solution model, it shows the two-phase region at room temperature. However, it has been proposed that solid solution phases exist at room temperature by Yamada et al. [4], which is consistent with the experimental phase boundary data. Therefore, it is necessary to define a modifiedregular solution model to fit the experimental data.

This modified regular solution model with a concentration dependent interaction parameterhas been successfully applied on both analytical calculations and phase-field models. The simulation results will be discussed.

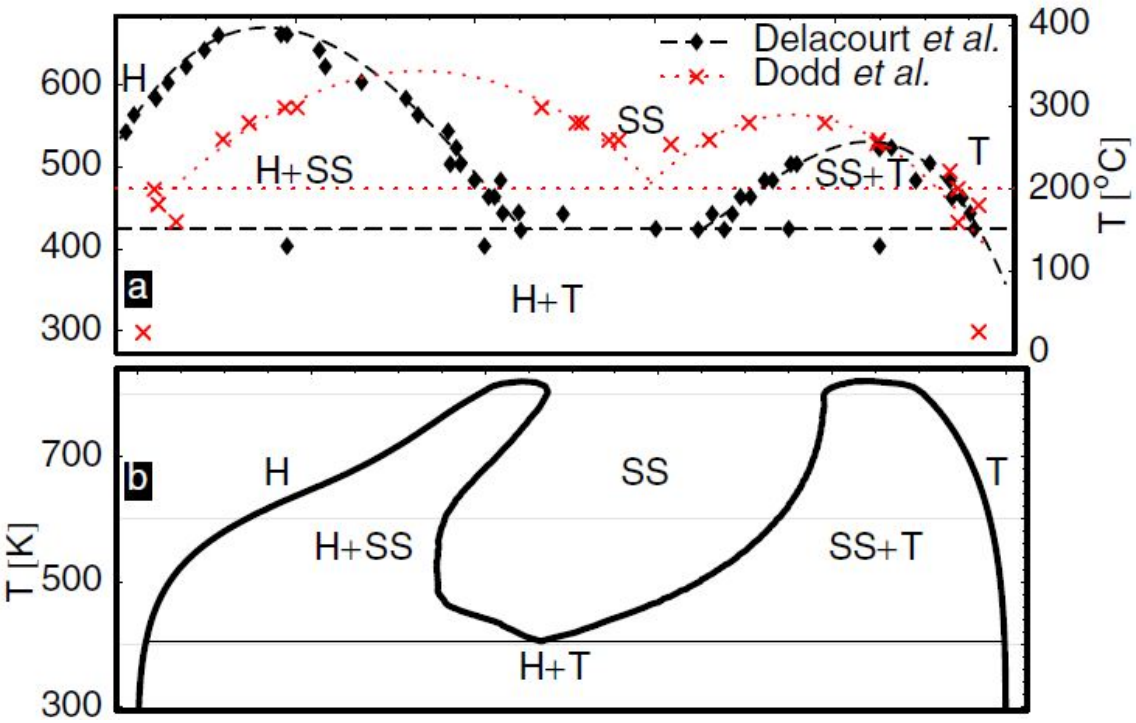

Fig. 4.1 (a) Experimental phase boundary data taken from Delacourt et al. [1] and from Dodd et al. [2]. (b) Calculated phase diagram from Zhou et al. [3].

4.2 Regular solution model with concentration dependent interaction parameter

The free energy expression of theregular solution model with a concentration dependent interaction parameter is shown in Eq. 4.1, which is calculated by finding the best fit free energy expression between two sets of the experimental data [1, 2]. Unlike the regular solution model from chapter 3 that Ω is related to the interaction strength between atoms, which is a constant equal to $59meV$ [5], Ω is a function of c_{Li} in thismodified regular solution model (4.2). And N_v is the number of the lithium atoms per unit cell volume, which is $1.37103\times10^{28}\left[1/m^3\right]$.

$$F(c,T)=N_v\left\{\left[\Omega(c)\right]c(1-c)+kT\left(c\ln c+(1-c)\ln(1-c)\right)\right\} \tag{4.1}$$

$$\Omega(c)=182.261-402.557c+875.534c^2-945.934c^3+461.415c^4 \tag{4.2}$$

The free energy plots at different temperatures are illustrated in Fig. 4.2. It shows the mostly miscibility gap at room temperature. Two common tangent lines can be drawn on Fig. 4.2 (b) which means there is a solid solution region between two two-phase regions at 520K. There is only one two-phase region at 600K, and the complete solid solution region shows at 700K.

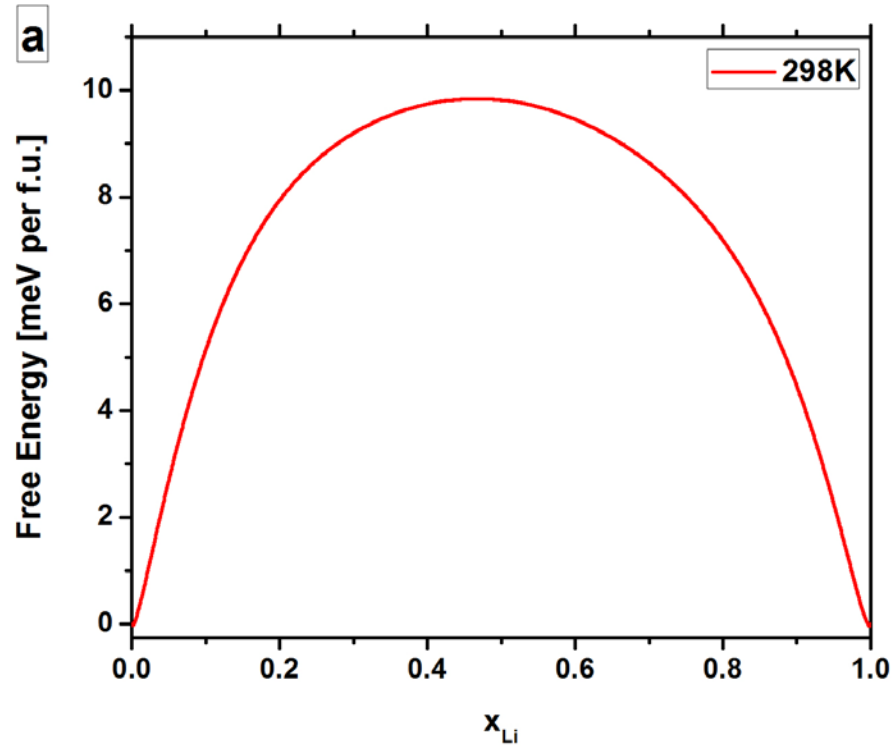
a
298K
Free Energy [meV per f.u.]
10
8
6
4
2
0
0.0
0.2
0.4
0.6
0.8
1.0
x_Li

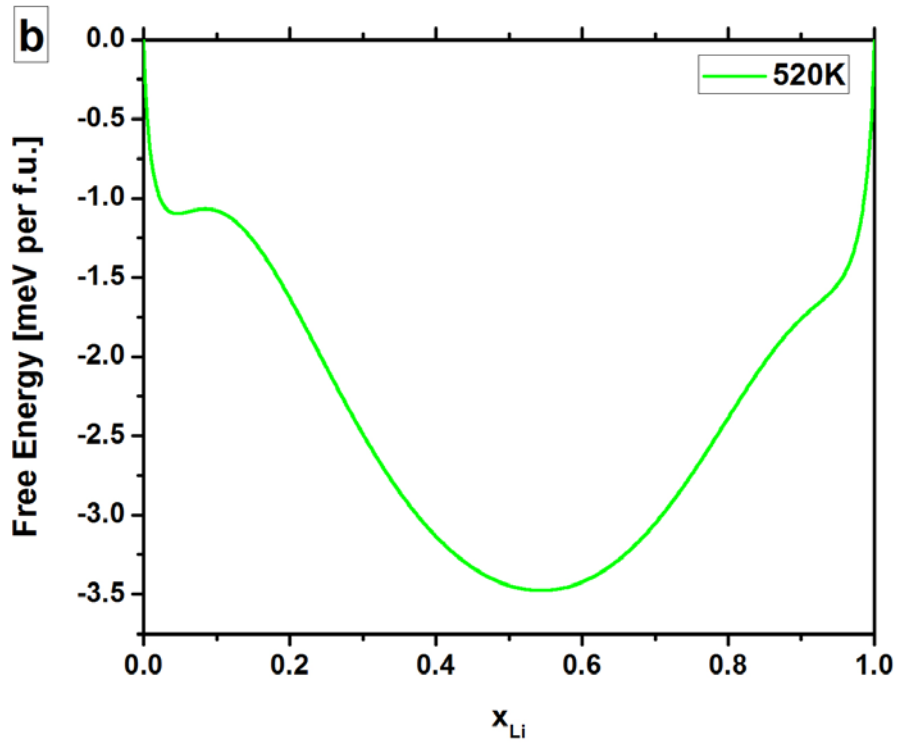
b
520K
Free Energy [meV per f.u.]
0.0
-0.5
-1.0
-1.5
-2.0
-2.5
-3.0
-3.5
0.0
0.2
0.4
0.6
0.8
1.0
x_Li

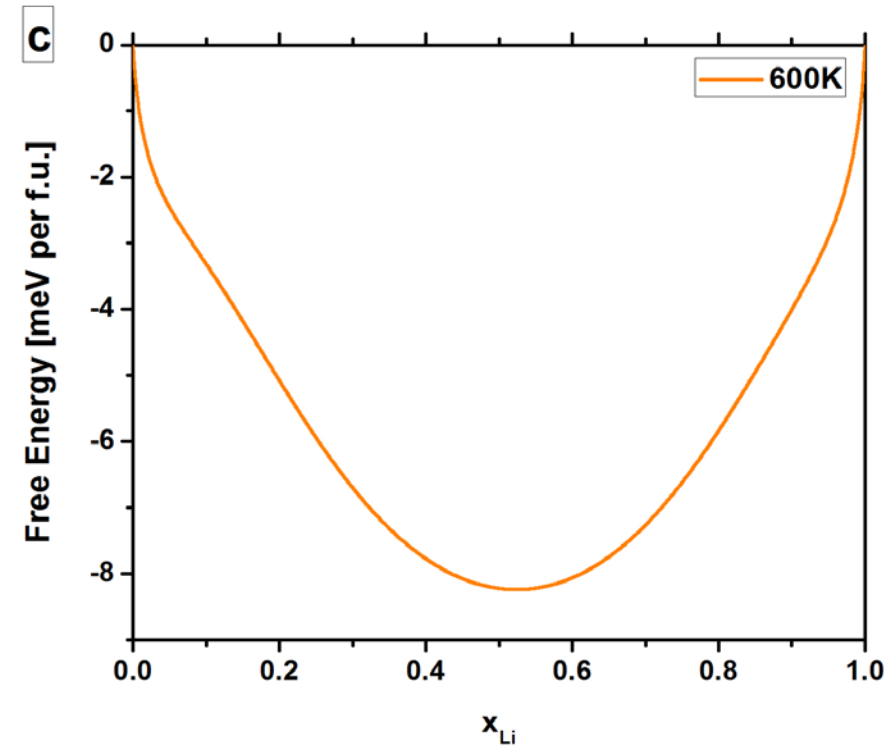
c
600K
Free Energy [meV per f.u.]
0
-2
-4
-6
-8
0.0
0.2
0.4
0.6
0.8
1.0
x_Li

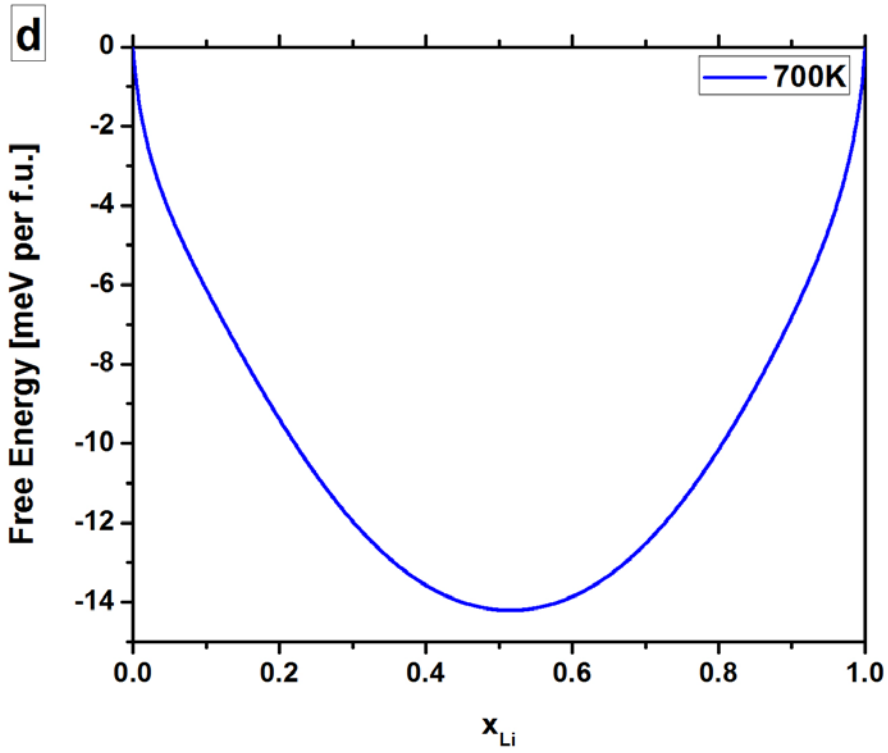
d
700K
Free Energy [meV per f.u.]
0
-2
-4
-6
-8
-10
-12
-14
0.0
0.2
0.4
0.6
0.8
1.0
x_Li

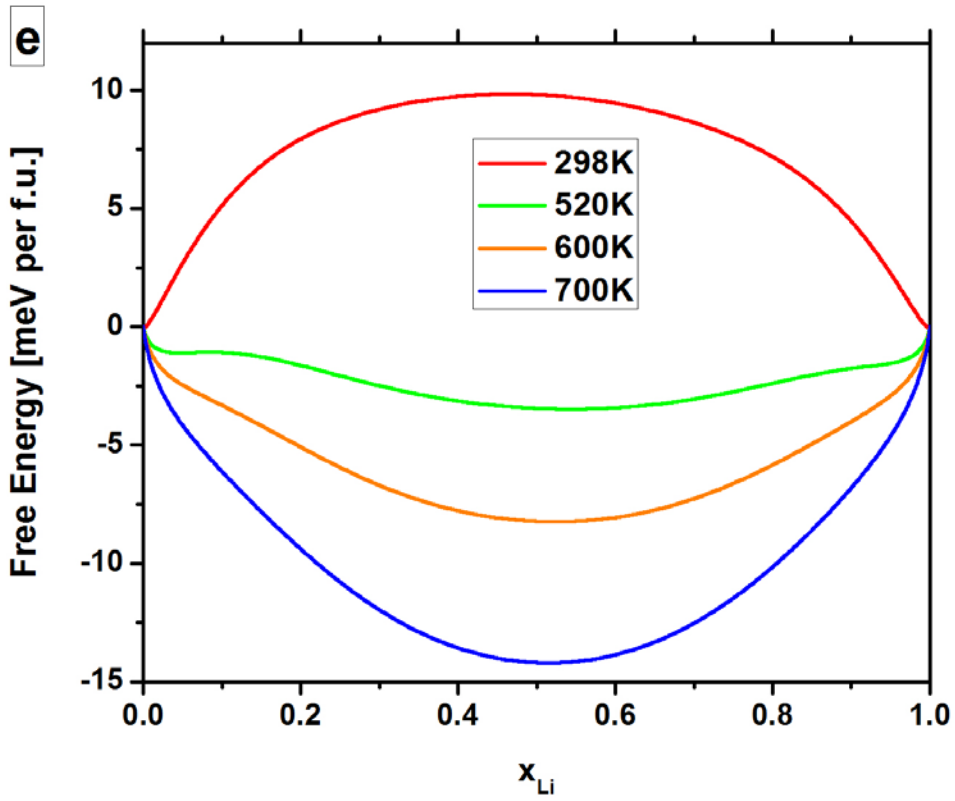

Fig. 4.2 (a) Fitted free energy of the regular solution model with a concentration dependent interaction parameter at room temperature, (b) at 520K, (c) at 600K, (d) at 700K; (e) All the free energy at different temperatures on the same plot.

Because it is not really clear if the experimental data corresponds to incoherent free energy, two possible phase diagrams can be obtained. First, assume experimental phase boundary data is showing the incoherent free energy. The phase diagram includes all different orientations that can be calculated showing in Fig. 4.3. At room temperature, all the phase boundaries (solid lines) that are including coherency strain energy effects are showing a solid solution region in the range around 0.3 to 0.7. This phase diagram explains why it has been proposed that solid solution phases exist at room temperature by Yamada et al. [4]. As lithium enters into iron phosphate, it starts from H region going through H+SS region, SS region and SS+T region. Finally, it ends in the T region. Most experiments are using $Li_{0.5}FePO_4$ as the sample, which is in the SS region to show the solid solution observation.

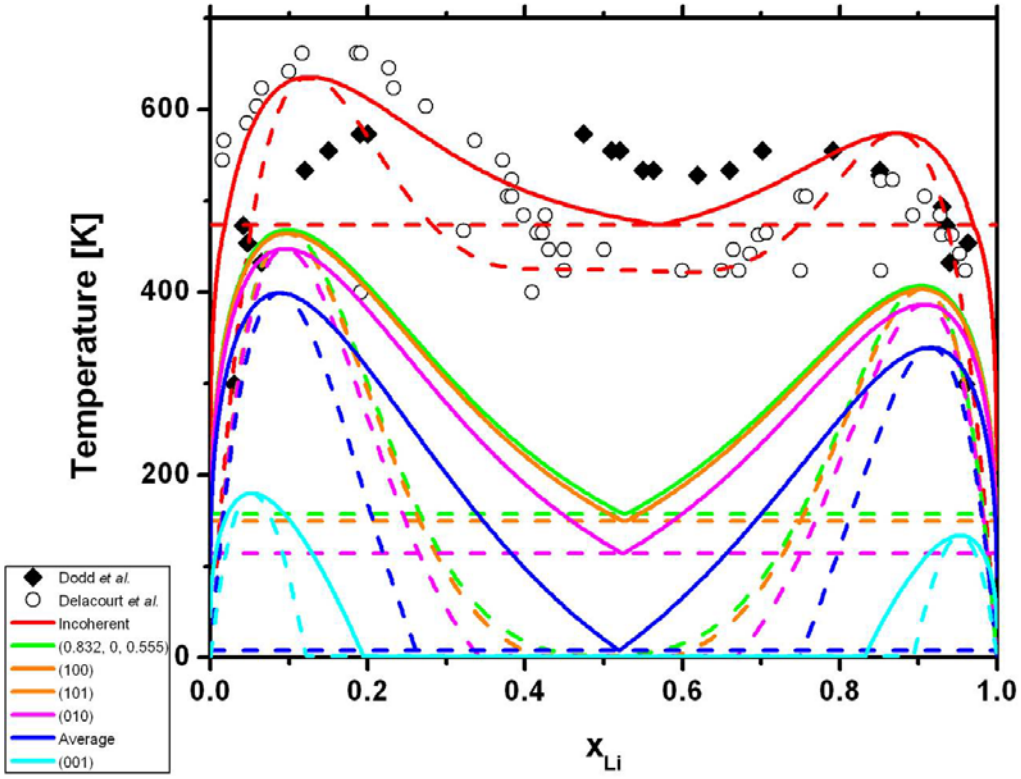

Fig. 4.3 Experimental phase boundaries data (Dodd et al. [2] and Delacourt et al. [1]) and calculated phase boundaries (solid lines), spinodal lines (dashed lines) and eutectic temperature (dashed lines) of the regular solution model with a concentration dependent interaction parameter of $FePO_4$-$LiFePO_4$ binary system for different habit planes by assuming experimental data does not include coherent strain energy contribution.

From Fig. 4.3, we can see the phase boundaries of (100) and (101) are very close to each other, therefore, it is not surprising that some experimental observations [6] showing (100) as preferred habit plane (Fig. 3.7) and some experimental observations [7] showing (101) habit plane is preferred (Fig. 4.4).

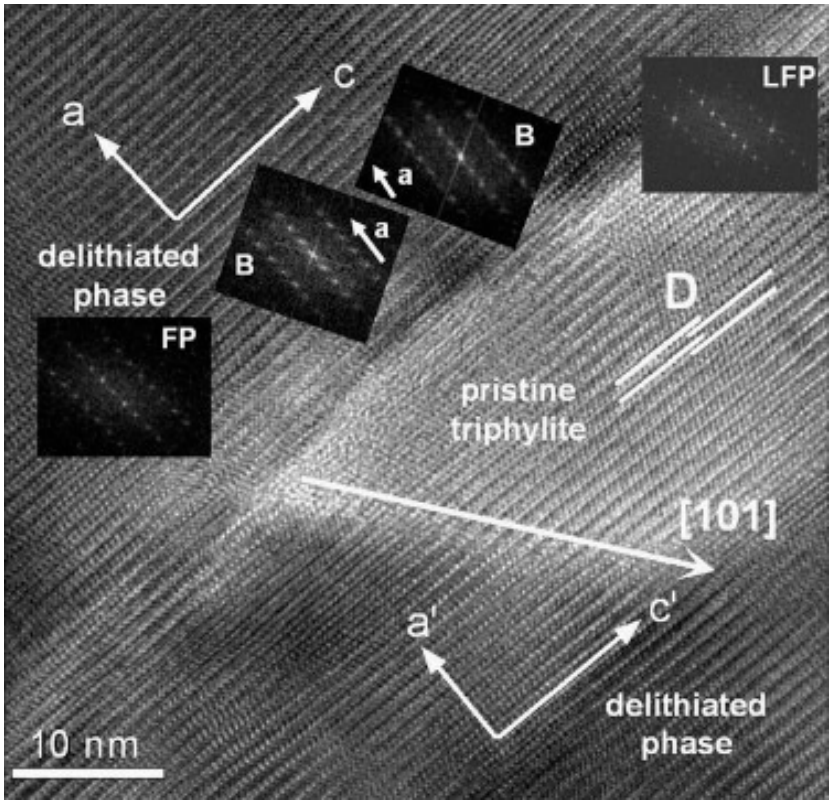

Fig. 4.4 HRTEM image of the 0.5($LiFePO_4$ + $FePO_4$) sample showing (101) habit plane.

Thus, we can make another assumption which is the experimental phase boundary data is showing the (100) or (101) habit plane coherent free energy. The phase diagram includes all the different orientations that can be calculated are shown in Fig. 4.5.

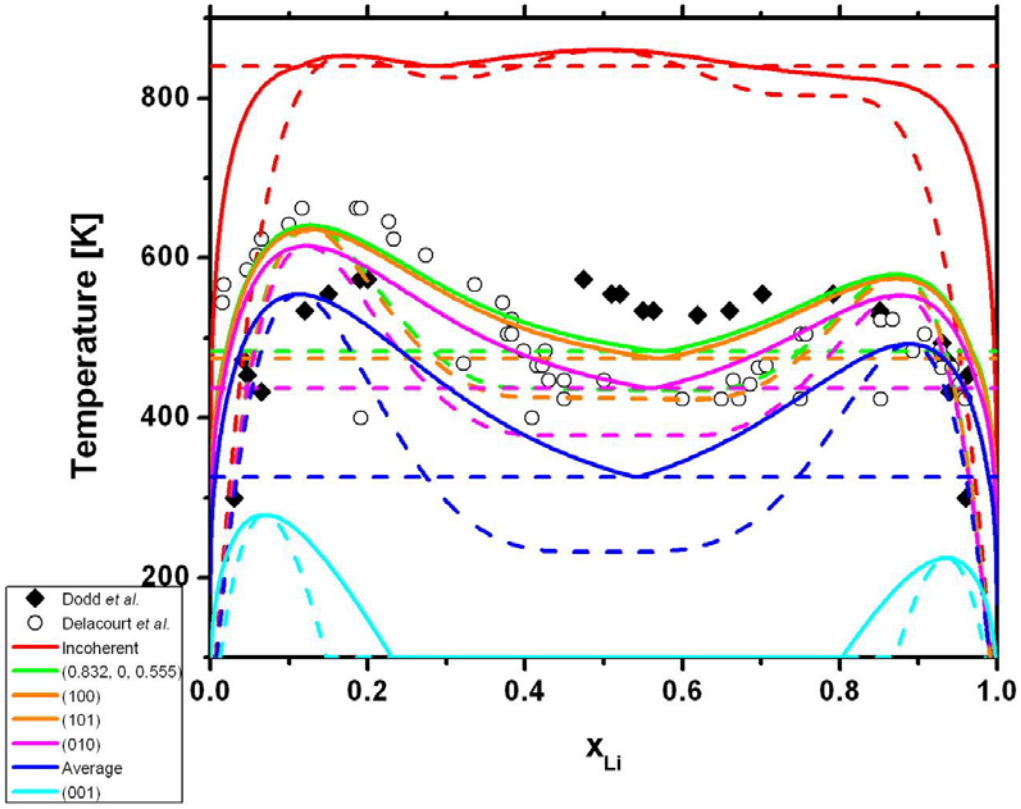

Fig. 4.5 Experimental phase boundary data (Dodd et al. [2] and Delacourt et al. [1]) and calculated phase boundaries (solid lines), spinodal lines (dashed lines) and eutectic temperature (dashed lines) of the regular solution model with a concentration dependent interaction parameter of $FePO_4$-$LiFePO_4$ binary system for different habit planes by assuming experimental data includes coherent strain energy contribution.

4.3 Phase-fieldsimulation results and discussion

The samephase-fieldmodel used for the regular solution model has been applied on the modified regular solution model with concentration dependent interaction parameter, where experimental data is observed including the contribution of coherent strain energy. In the phase-field simulations, we also employed $64\times64\times64$ three dimensional discrete grid points, and periodic boundary conditions along all the directions with the time step for integration is $dt = 0.0005$. The gradient coefficient is $\kappa = 0.25$ and initial concentration is $c_0 = 0.5$. As expected, the strong anisotropic elasticity with preferred habit plane is shown in the simulation results (Fig. 4.6) at 350K due to spinodal decomposition.

Fig. 4.6 Three dimensional morphology of the regular solution model with a concentration dependent interaction parameter at 350K.

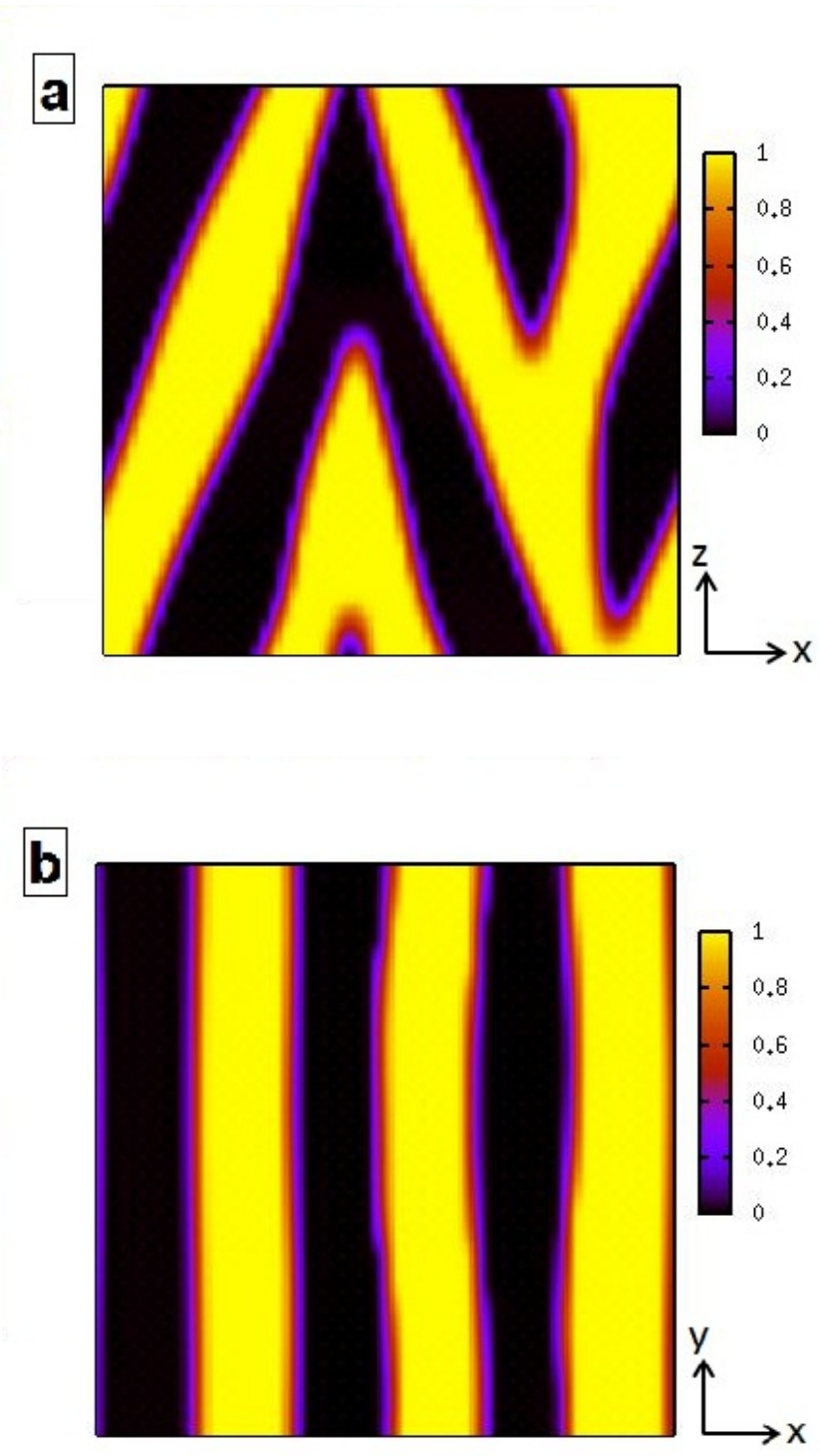

Fig. 4.7 (a) x-z cross sectional face and (b) x-y cross sectional face of three dimensional morphology of the regular solution model with a concentration dependent interaction parameter at 350K.

In the same way as Fig. 3.6 (b), Fig.4.7 (b) shows the habit plane is along the y direction, which is consistent to our calculation. The determined habit plane needs to be converted into an orthorhombic system (3.14) by using the experimental lattice parameters [6] since there areperiodic boundary conditions along all the directions in the simulation.

The determined habit plane is (0.825, 0, 0.565) after conversion, which has 0.85% difference in x direction and 1.77% difference in z direction compared with calculated habit plane (0.832, 0, 0.555). This excellent agreement between theoretical calculations and simulations indicate the optimum habit plane is preferred. As we discussed in the previous chapter, the (100) habit plane (Fig. 3.7) [6] and (101) habit plane (Fig. 4.4) [7] have been observed in some experiments. First, both (100) habit plane and (101) habit plane are able to be observed in the experiments since they have extremely close total free energy. A possible reason the optimum habit plane was not observed in an experiment is due to defects which could partially lose coherency energy to show the minimum total energy, and also (100) may show lower interfacial energy than the optimum habit plane which gives the lowest total energy contribution.

4.4 Summary

In summary, the modified regular solution model with a concentration dependent interaction parameter is developed to match with the experimental phase boundary data. The calculated phase diagram and three dimensional phase-field simulations are shown in the chapter by combining the phase-field method with microelasticity theory. The excellent agreement between theoretical calculations and simulations show the optimum habit plane is preferred if only considering coherency strain energy effects.

References

[1] C. Delacourt, P. Poizot, J. –M. Tarascon, and C. Masquelier, *Nature Materials* **4**, 254-260 (2005).

[2] J. L. Dodd, R. Yazami, and B. Fultz, *Electrochemical and Solid-State Letters* **9**, A151-A155 (2006).

[3] F. Zhou, T. Maxisch, and G. Ceder, *Physical Review Letters* **97**, 155704 (2006).

[4]A. Yamada, H. Koizumi, N. Sonoyama, and R. Kanno, *Electrochemical and Solid-State Letters***8**, A409 (2005).

[5] B. C. Han, A. Van der Ven, D. Morgan, and G. Ceder, *ElectrochimicaActa***49**, 4694-4695 (2004).

[6]G. Chen, X. Song, and T. J. Richardson, *Electrochemical and Solid-State Letters***9**, A296 (2006).

[7] C. V. Ramana, Z. Mauger, F. Gendron, C. M. Julien, and K. Zaghib, *Journal of Power Sources***187**, 555-564 (2009).

CHAPTER 5

PHASE-FIELD MODELING OF LITHIUM INTERCALATION IN LI-ION BATTERY CATHODE

5.1 Spectral smoothed boundary methods

The spectral smoothed boundary method is considered a powerful tool for solving variouspartial differential equations, since it can generally impose the boundary conditions in the interested domain [1].This method is based on a diffuse interface description of different phases, which is very similar to the continuously transitioning order parameters in the phase-field approach used in studying phase transformationsand microstructural evolution in materials. The phase-field method has been described at length in the previous chapter. This method has the benefit of avoiding the need to solve for the boundary conditions explicitly. The spectral method is frequently used because of its ability to discretize spatial variables in partial differential equations. The most substantial benefit from this method is accurate approximations of smooth solutions to higher-order problems. The solutions have high-order accuracy, which makes them practical models for many different applications.

The primary competing method with the spectral method of analyzing partial differential equations is finite-difference or finite-element methods. The reason for this is that spectral methods on their own are able to solve linear and nonlinear equations, but only by using full matrices. These matrices require large amounts of computing power and time in order to complete the immense number of computations necessary. Finite-element methods, on the other hand, only require partial, instead of full, matrices. This means the calculations can be performed in a much simpler manner requiring less time, making it a more feasible method for many types of calculations as opposed to the spectral method. Another reason the use of the spectral method on its own is limited in the areas that it can provide effective solutions is that it does not work well with irregularly shaped domains. The problem domain must have a simple geometry that can be modeled without preconditioning. This is especially important when using Fast Fourier Transforms with the spectral method.

The spectral smoothed boundary method provides improvements over the use of the spectral method on its own that allow the approximation of solutions of partial differential equations with complex domains. This method implements ideas from phase-field methods, which allows the spectral method to be used in a wider range of applications. The spectral smoothed boundary method is based in the use of the phase-field method, specifically with Neumann boundary conditions, to partial differential equations. The smoothed boundary method does not discretize the problem; it sets up a function that is one inside the domain and continuous and smoothly decays to zero outside the domain. The significance of this is that on an enlarged domain (Ω') that contains the original irregular domain (where Ω exists on Ω'), the solutions automatically

incorporate the boundary conditions. Thus, the smoothed boundary method has created a way for complex boundary conditions to be solved with the spectral method.

The original phase-field equation can be rewritten and assuming $\partial_t \phi = 0$, simplified to [1]

$$\nabla \log \phi \cdot D\nabla u + \nabla(D\nabla u) + f(u,t) = \partial_t u. \tag{5.1}$$

This equation can then be used to run numerical simulations for a variety of applications. This still requires the use of a smooth characteristic function before it can be implemented. The typical phase-field method is to integrate an auxiliary equation until it reaches a steady state. To obtain a smooth boundary only a form of χ is needed to satisfy the initial condition $\phi^{(\xi)}(t=0) = \chi_\Omega$. This can be accomplished using a form of the equation [1],

$$\phi^{(\xi)} = \chi_\Omega * G^{(\xi)}, \tag{5.2}$$

where$G^{(\xi)}$ can be expressed as $\lim_{\xi \to 0} G^{(\xi)}(x) = \delta(x)$.

The use of the spectral smoothed boundary method employs the Fourier Transforms to complete its calculations. This effectively eliminates the need for differentiation matrices, which require time and space for their creation and storage. Fast Fourier Transforms can also be used to speed this process up further, resulting in more

efficient systems. The enlarged domain is created with a normal shape and boundary conditions containing the irregular domain and is defined on a Cartesian grid that allows the spatial derivatives to be accurate in Fourier space. Other techniques are also used to enhance the effectiveness of the method, such as integrating the linear part of the equation with regards to Fourier space, which allows for larger time steps to be used.

This method is practical for solving many types of problems. A simple example is a linear heat equation. In this case the equation is [1]

$$\partial_t u = D\Delta u - r\cos(2\theta), \tag{5.3}$$

in the annulus defined by the domain$1 \leq r \leq 2$and homogeneous Neumann boundary conditions. This form of the equation is used because a solution can be found explicitly and the results of the spectral smoothed boundary method can be compared to a known, accurate value. The relative error the method produces can then be observed. The relative error produced by the simulation was less than 1%. The results also show that as the resolution at the edge of the domain is increased, the errors decrease. This increase in resolution is provided by decreasing the thickness of the interface, the area where the function decays from 1 to 0. The amount of error is primarily due to grid refinement in this area, not in the refinement of the entire domain. It is also important to note that these errors occur because of discretized spatial points created by the simulation.

The spectral smoothed boundary method provides an improvement in its ability to produce an accurate solution even with sharp corners or other irregular domain shapes. The case studied by [1] tested a quarter-annulus because of its sharp corners. The result was a solution similar to the case of a full annulus, with slightly larger errors, especially at the sharp corners. The method did not function with complete accuracy but represents a highly accurate simulation of the problem.

The other major benefit of using this method comes from the smoothed boundary equation used to perform the simulation. This equation is able to account for changes in the boundary conditions in a much easier to use manner. Instead of creating and computing separate equations for each boundary condition, the formula is able to adapt to changes automatically. This reduces the complexity of the problem, and creates high degrees of accuracy even where analytic solutions are not possible. This method is able to surpass the accuracy of finite element models, especially in higher-order problems. An example is in a case where polar and Cartesian coordinates are used in the domain geometry. The grid used for the finite element model must be extremely fine in order to approximate the solution given by spectral smoothed boundary methods, making that method less feasible.

The use of Fast Fourier Transforms in these types of problems increases the efficiency of this method. It is also simple to implement FFTs for most models, since every step has been in compliance with Fourier space. The limiting factor is the need to use large numbers of points to solve problems without steep boundary slopes. In problems that do have steep slopes or gradients the method is accurate and requires the same resolution as other methods. Fast Fourier can be used for any type of boundary

condition; periodic, homogeneous Dirichlet, or homogeneous Neumann. The difference between these is in the computation of the external boundary conditions. The area computed inside the irregular domain is the same regardless, with any differences attributed to different wave velocities based on the amount of points used to compute the spatial derivatives [2].

5.2 Smooth boundary and phase-field model

According to many published papers and first-principle calculations, Li diffusion occurred in almost one-dimension in the olivine structure.The diffusivity of Li-ion is faster along [010] direction than [100] and [001] direction due to the much lower migration energy in [010] direction and higher activation energies in the [100] direction and [001] direction, which is supported by the experiment of Nishimura et al. [3]. The diffusion coefficients of Li were measured in the range of 10^{-12}-$10^{-17}$$cm^2s^{-1}$ by Amin et al. [4, 5].

In order to model the different effects in lithium iron phosphate ($LiFePO_4$), the phase-field model using smooth boundary method has been modified. The phase-field model we built is designed to show the mesoscale $LiFePO_4$nanoparticle morphology trends with different parameters by using the regular solution model. In our simulations, we specify all parameters to be dimensionless. We first choose an order parameterξ to define the two different domains; nanoparticle domain and matrix domain. The nanoparticle inside the domain (circle) is denoted by$\xi = 1$ and the matrix is denoted by$\xi = 0$, respectively. We choose a circle domain with particle radius r = 65 in the center

of the simulation box to represent a $LiFePO_4$nanoparticle. Then we smooth the domain boundary to generate a diffuse interface, which allows us to use the spectral smoothed boundary method to specify the Neumann's boundary condition. After we smoothed the domain boundary, we fix the boundary of the domain and do not evolve it with time. We are just interested in the changes of properties inside the domain. In this work, wemainly focus on the phase transitions and morphology of microstructure in a nanoparticle in the lithium-ion cathode due to the lithium diffusion process.

5.3 Concentration effects on the morphology

We first studied the effect of different initial concentrations of lithium inside of the domain under the other fixed parameters. Three examples have been chosen with the initial concentrations $C_0 = 0.3$, $C_0 = 0.5$, and $C_0 = 0.7$. The phase-field simulation results of these cases are shown in Fig. 5.1 to Fig. 5.3. The different colors in the figure represent the different lithium concentrations. The scale bar next to each square indicates the value of lithium concentration. As the lithium concentration goes from low to high, the color goes from dark to bright. We specify the lithium flux as a boundary condition on the particle surface, which corresponds to the production of the electrochemical reaction. In Fig. 5.1, when$t^* = 0$, the purple circle in the black box means the initial concentration inside the domain is 0.3. As the time steps increase, the lithiumstarts to go inside the $FePO_4$nanoparticle from the particle surfaceas seen in Fig. 5.1 (c). The lithium starts to fill up the particle from the surface slowly. It gives an almost core-shell morphology of nanoparticle, which is consistent with previous models [6]. Finally, the

nanoparticle is full of lithium equilibrium concentration, which illustrates the discharging process of the battery.

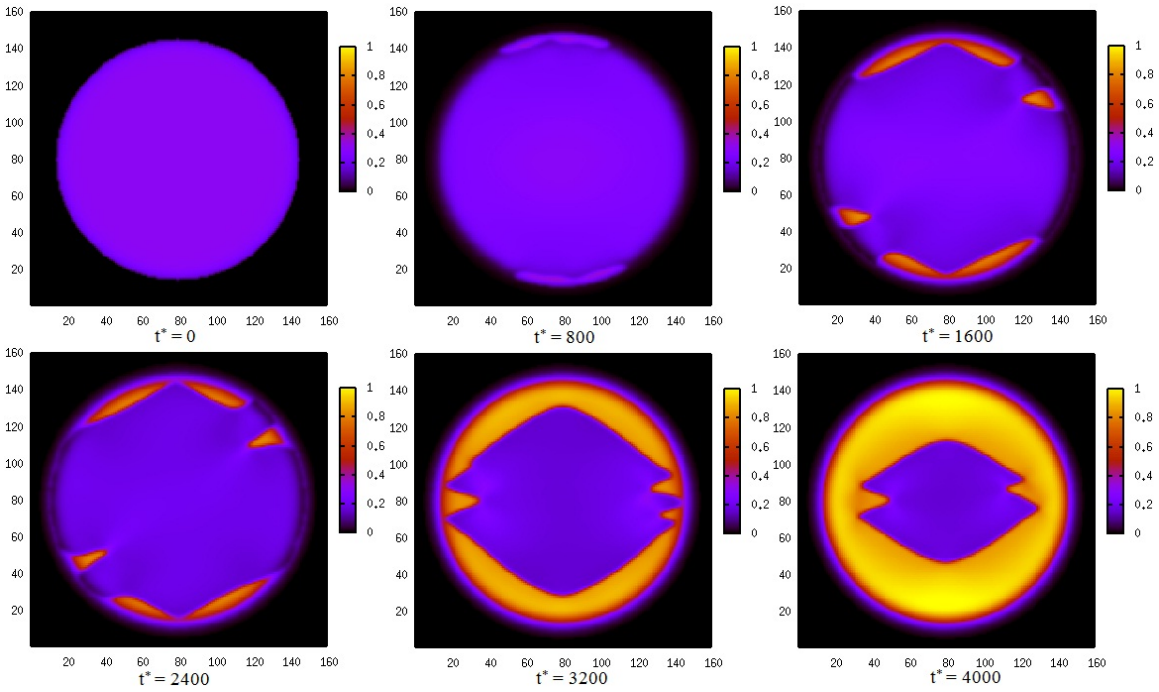

Fig.5.1 Lithium concentration (initial concentration, $C_0 = 0.3$) evolution with different time steps and isotropic mobility under fixed overpotential ($\eta = 0.03$) in a selected size nanoparticle in the Li-ion battery cathode.

Fig. 5.2 shows the phase-field simulation results with initial concentration $C_0 = 0.5$. The spinodal decomposition can be observed, which means it separates into two distinct phases, i.e.,lithium-poor phase and lithium-rich phase. Beside the

spinodaldecomposition effects on the morphology, the misfit strain between two phases can also affect the lithium diffusion process in the particle, which gives an aligned morphology for the microstructure. Since we impose a lithium flux boundary condition on the surface with overpotential$\eta = 0.03$, the lithium concentration increases with the increased time steps. In the end, the lithium concentration inside the particle reaches the equilibrium concentration and the nanoparticle is full of lithium.

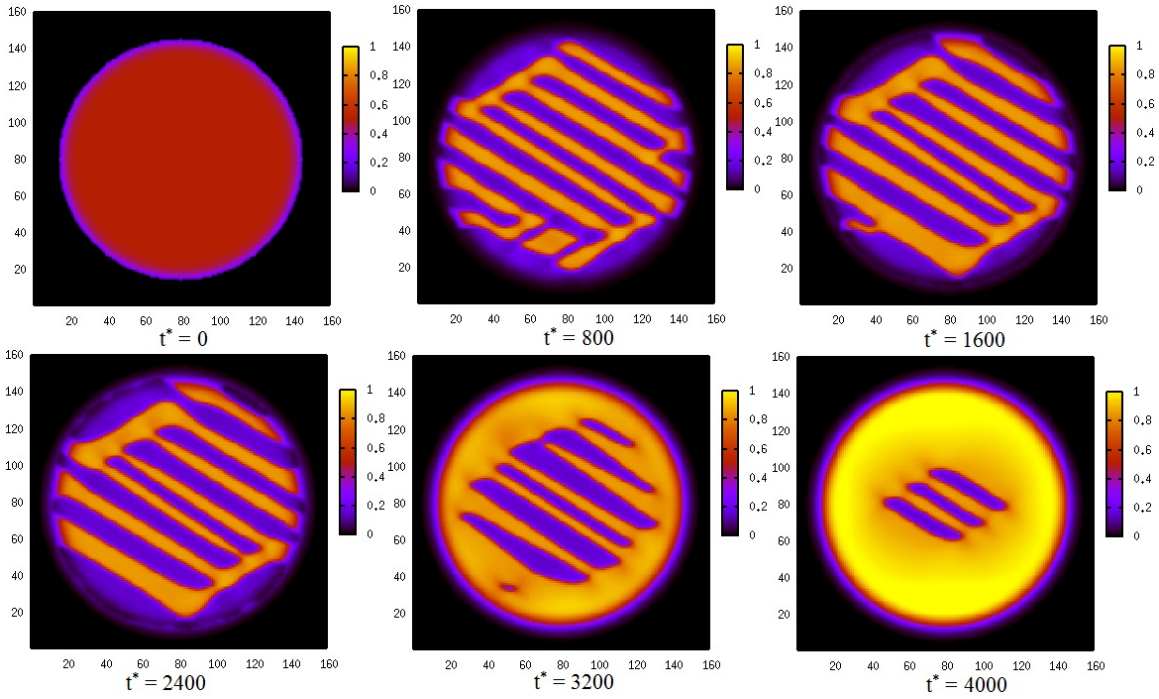

Fig.5.2 Lithium concentration (initial concentration, $C_0 = 0.5$) evolution with different time steps and isotropic mobility ($m_{xx} = 1, m_{yy} = 1$) under fixed overpotential ($\eta = 0.03$) in a selected size nanoparticle in the Li-ion batterycathode.

In Fig. 5.3, it clearly shows that the lithium concentration increases much faster with the initial concentration $C_0 = 0.7$ than the lower initial concentration cases. The simulation results show the trend of increasing lithium concentration as in previous cases. The misfit between two phasesproducesan aligned microstructure. However, the morphology of the microstructure is very different from the lower initial concentration cases. In this case, it is considered that the initial lithium concentration plays a more important role in the morphology of the microstructure.

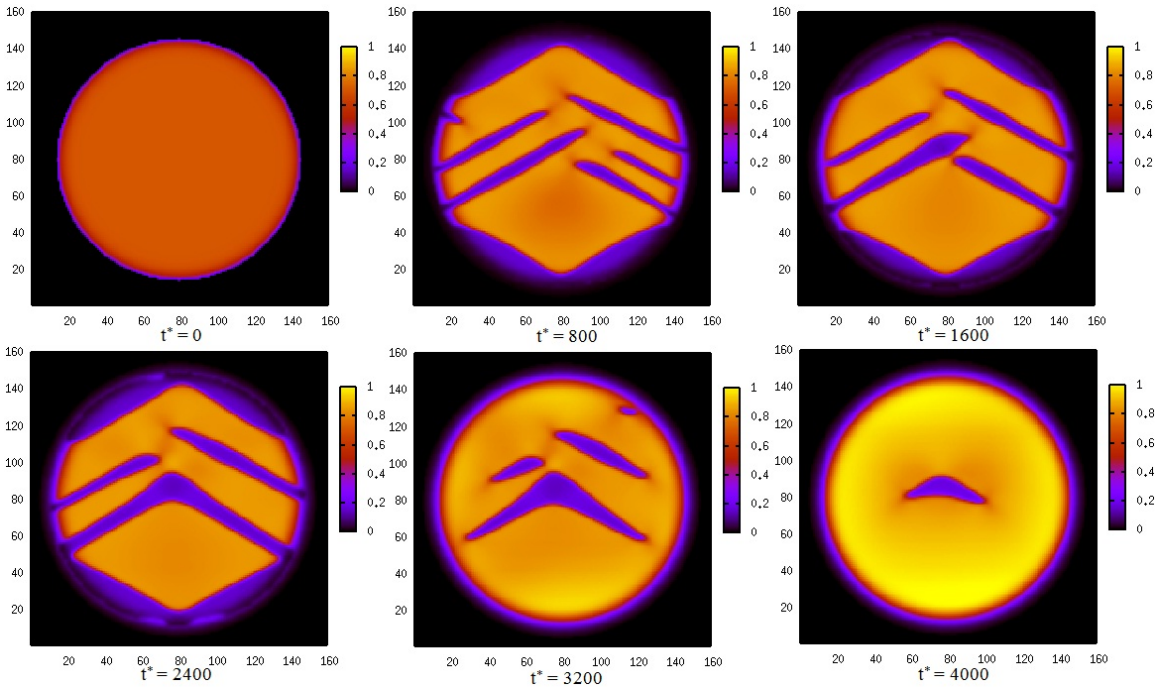

Fig.5.3 Lithium concentration (initial concentration, $C_0 = 0.7$) evolution with different time steps and isotropic mobility ($m_{xx} = 1, m_{yy} = 1$) under fixed overpotential ($\eta = 0.03$) in a selected size nanoparticle in the Li-ion battery cathode.

5.4 Overpotential effects on the morphology

The overpotential isrelated to the lithium flux going inside or outside the nanoparticle. With the larger overpotential, we could get the higher lithium flux. Then we studied the effects of the different overpotentialon the microstructure evolution under the fixed initial concentration $C_0 = 0.3$ and isotropic mobility condition. We select three different overpotential cases,$\eta = 0.02$, $\eta = 0.04$, and $\eta = 0.06$, which correspond to Fig. 5.4 to Fig 5.6.As can be seen in the figures, the lithium diffuses into the domain from the particle surface grows faster withthe increasing of overpotential. This is similar to the faster discharging process in the battery with the higher overpotential. The morphology of the microstructure also illustrates a core-shell structure at three given different overpotentials.

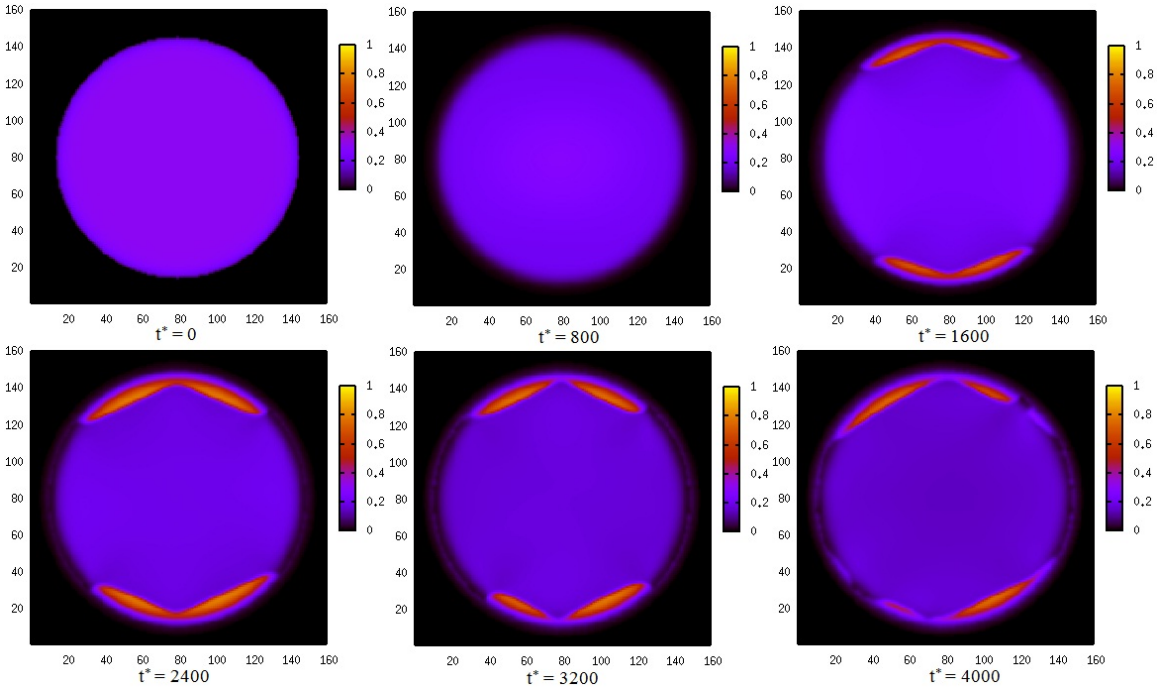

Fig.5.4 Lithium concentration evolution with different time steps and isotropic mobility ($m_{xx} = 1, m_{yy} = 1$) at overpotential equal to 0.02 ($\eta = 0.02$) under fixed initial concentration ($C_0 = 0.3$) in a selected size nanoparticle in the Li-ion battery cathode.

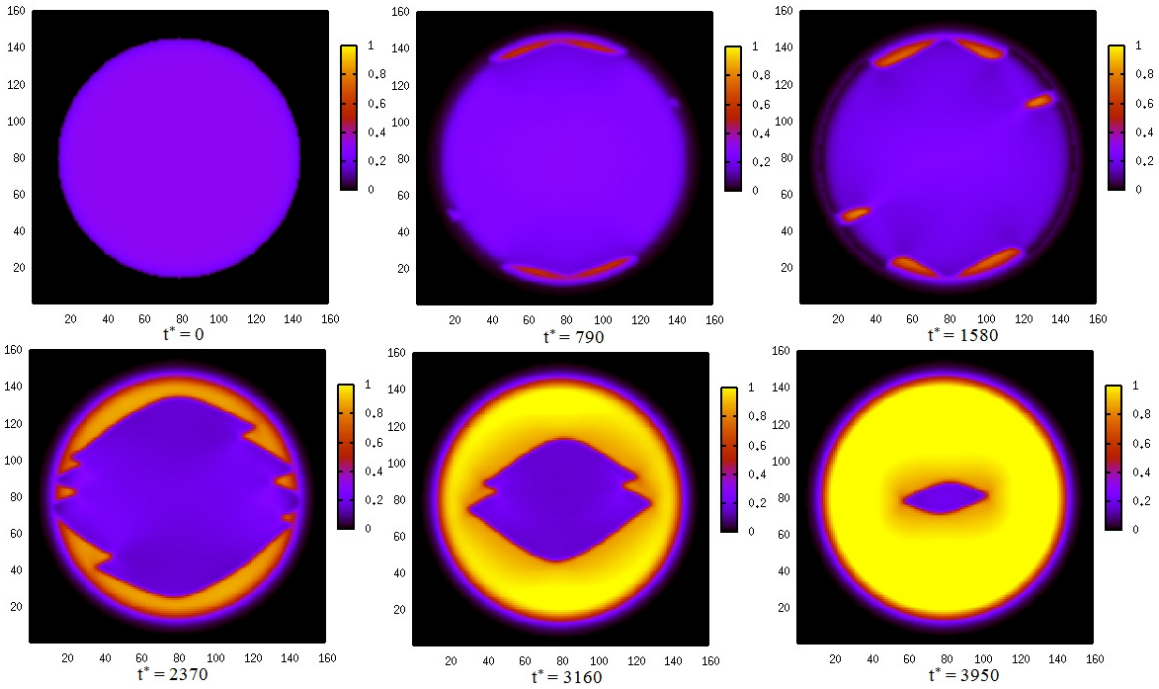

Fig.5.5 Lithium concentration evolution with different time steps and isotropic mobility ($m_{xx} = 1, m_{yy} = 1$) at overpotential equal to 0.04 ($\eta = 0.04$) under fixed initial concentration ($C_0 = 0.3$) in a selected size nanoparticle in the Li-ion battery cathode.

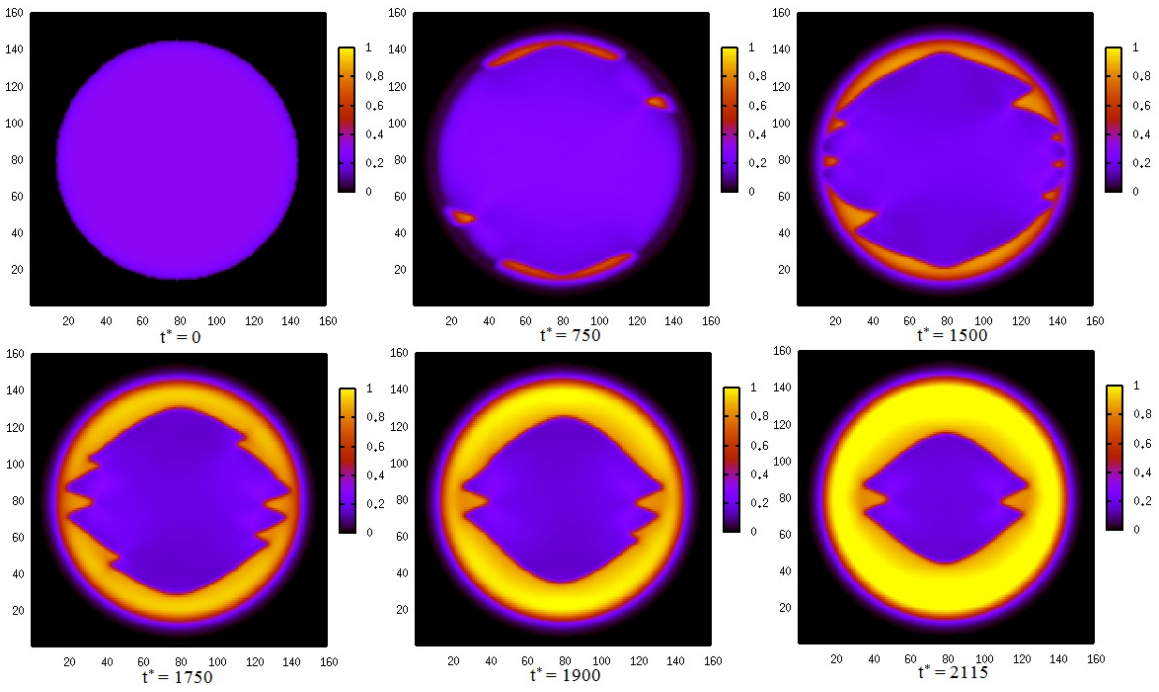

Fig.5.6 Lithium concentration evolution with different time steps and isotropic mobility ($m_{xx} = 1, m_{yy} = 1$) at overpotential equal to 0.06 ($\eta = 0.06$) under fixed initial concentration ($C_0 = 0.3$) in a selected size nanoparticle in the Li-ion battery cathode.

We fix the initial concentration to be 0.4 with the variation of overpotential$\eta = 0.02$, $\eta = 0.04$, and $\eta = 0.06$. This initial concentration is in the spinodal decomposition region based on the free energy formulation. It is shown in Fig. 5.7 to Fig 5.9 that the initial uniform lithium concentration decomposes into higher and lower equilibrium concentration, i.e. lithium-poor and lithium-higher phases. The higher overpotential induces a faster discharging process. Compared with the lower initial concentration cases, the spinodal decomposition plays a main role in forming the morphology of the microstructure of the nanoparticle.

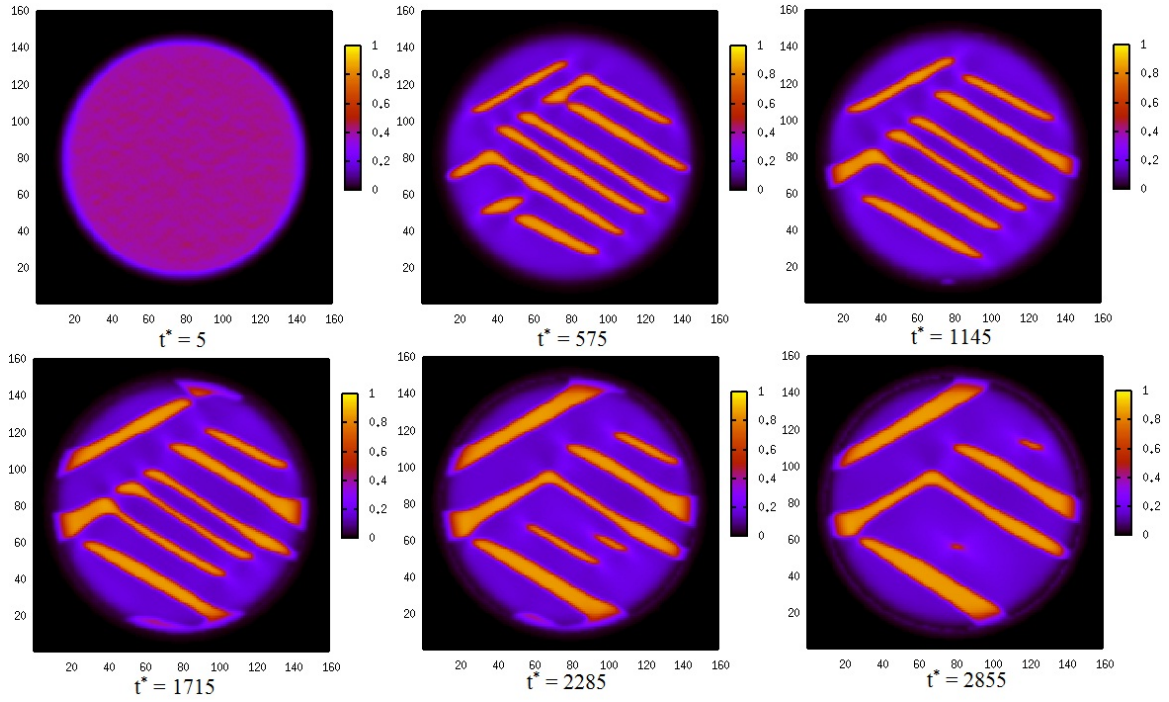

Fig.5.7 Lithium concentration evolution with different time steps and isotropic mobility ($m_{xx} = 1, m_{yy} = 1$) at overpotential equal to 0.02 ($\eta = 0.02$) under fixed initial concentration ($C_0 = 0.4$) in a selected size nanoparticle in the Li-ion battery cathode.

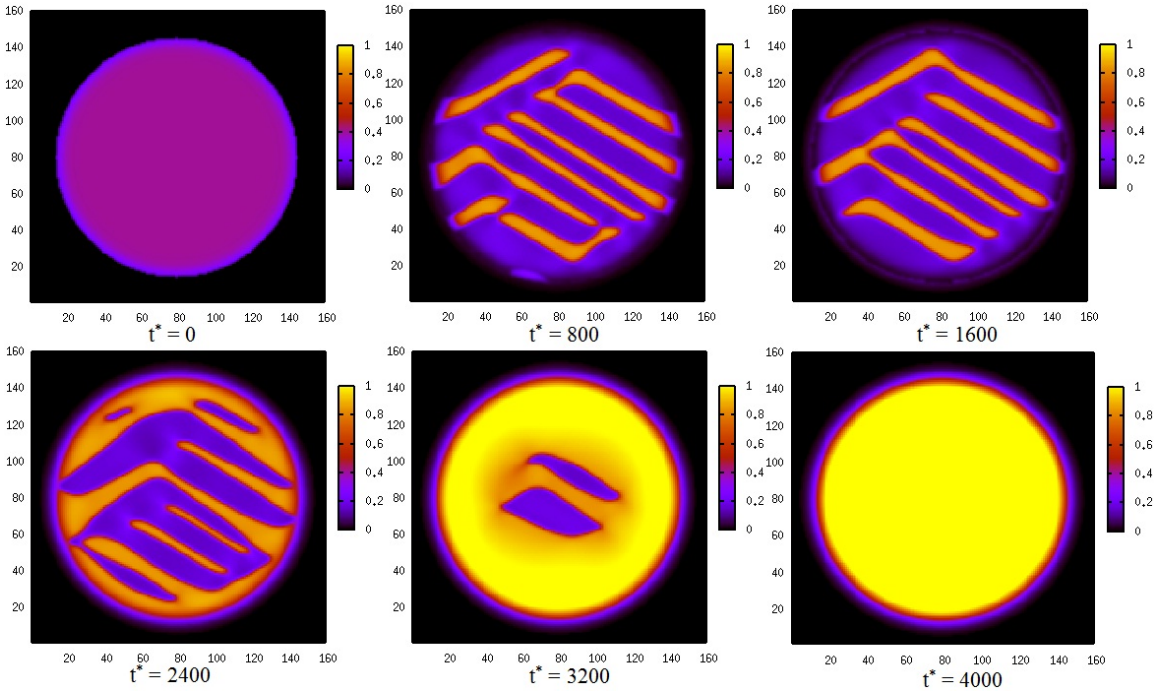

Fig.5.8 Lithium concentration evolution with different time steps and isotropic mobility ($m_{xx} = 1, m_{yy} = 1$) at overpotential equal to 0.04 ($\eta = 0.04$) under fixed initial concentration ($C_0 = 0.4$) in a selected size nanoparticle in the Li-ion battery cathode.

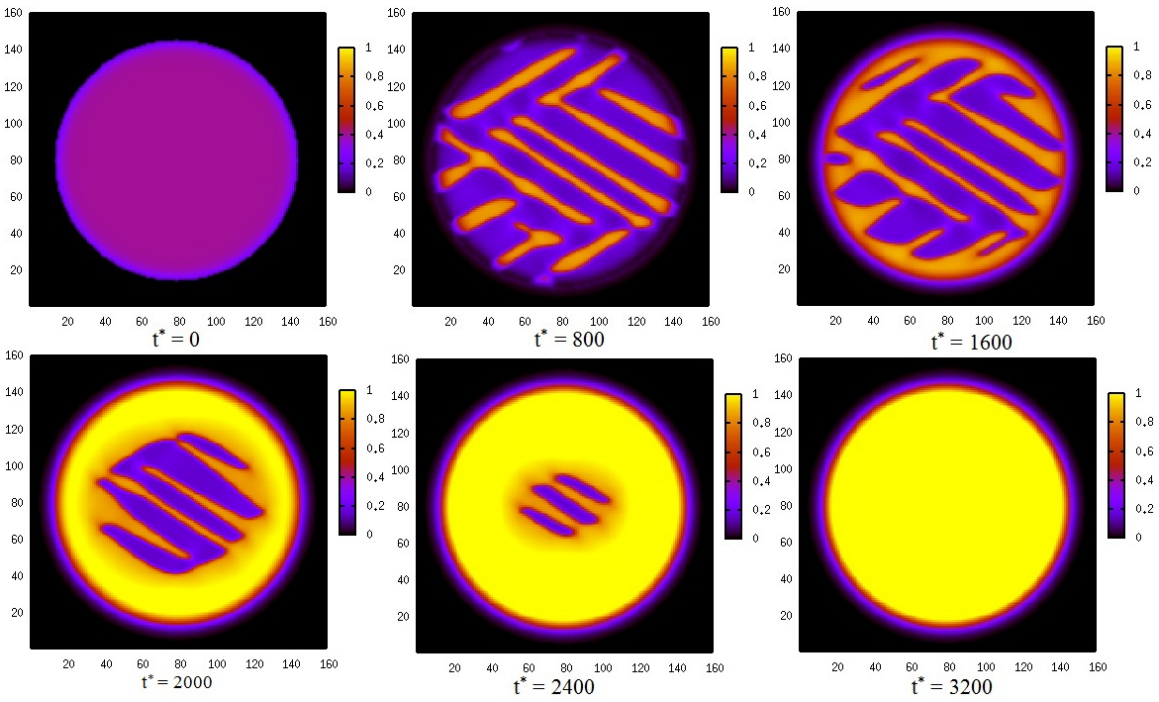

Fig.5.9 Lithium concentration evolution with different time steps and isotropic mobility ($m_{xx} = 1, m_{yy} = 1$) at overpotential equal to 0.06 ($\eta = 0.06$) under fixed initial concentration ($C_0 = 0.4$) in a selected size nanoparticle in the Li-ion battery cathode.

In Fig. 5.10 to Fig 5.12, we fix the initial concentration to 0.7 and study the effects of different overpotential $\eta = 0.02$, $\eta = 0.04$, and $\eta = 0.06$ on the lithium diffusion process.It is shown that the higher initial lithium concentration with different overpotential case illustrates that the misfit strain effects dominate the morphology of the microstructure.

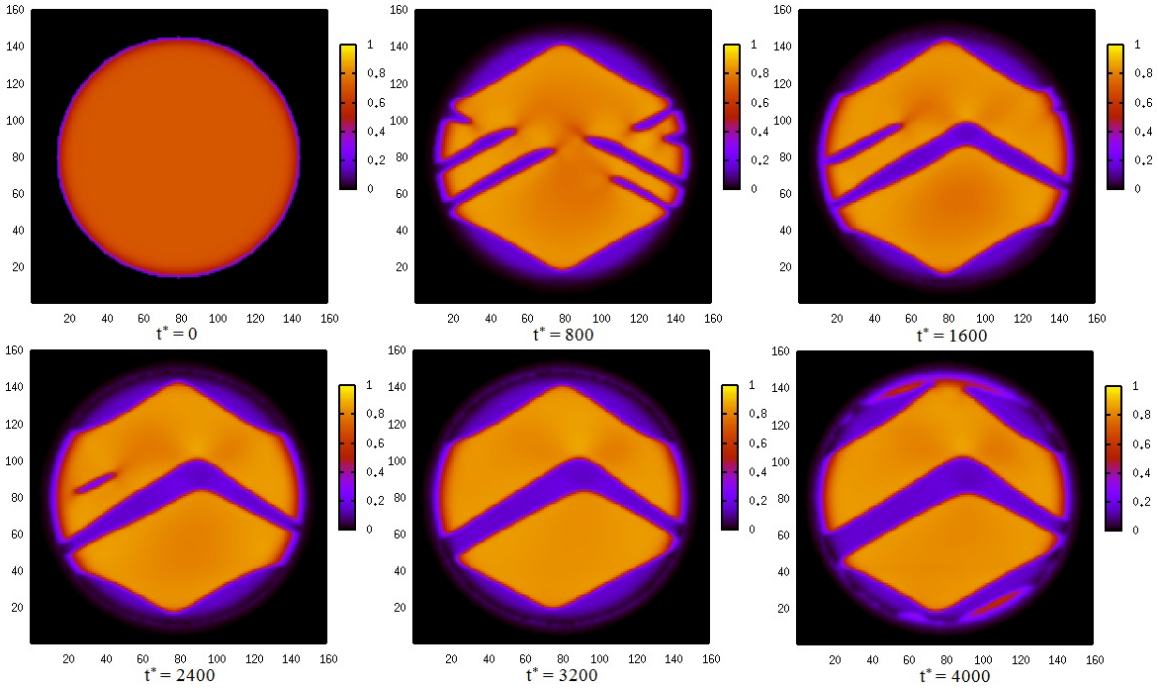

Fig.5.10 Lithium concentration evolution with different time steps and isotropic mobility ($m_{xx} = 1, m_{yy} = 1$) at overpotential equal to 0.02 ($\eta = 0.02$) under fixed initial concentration ($C_0 = 0.7$) in a selected size nanoparticle in the Li-ion battery cathode.

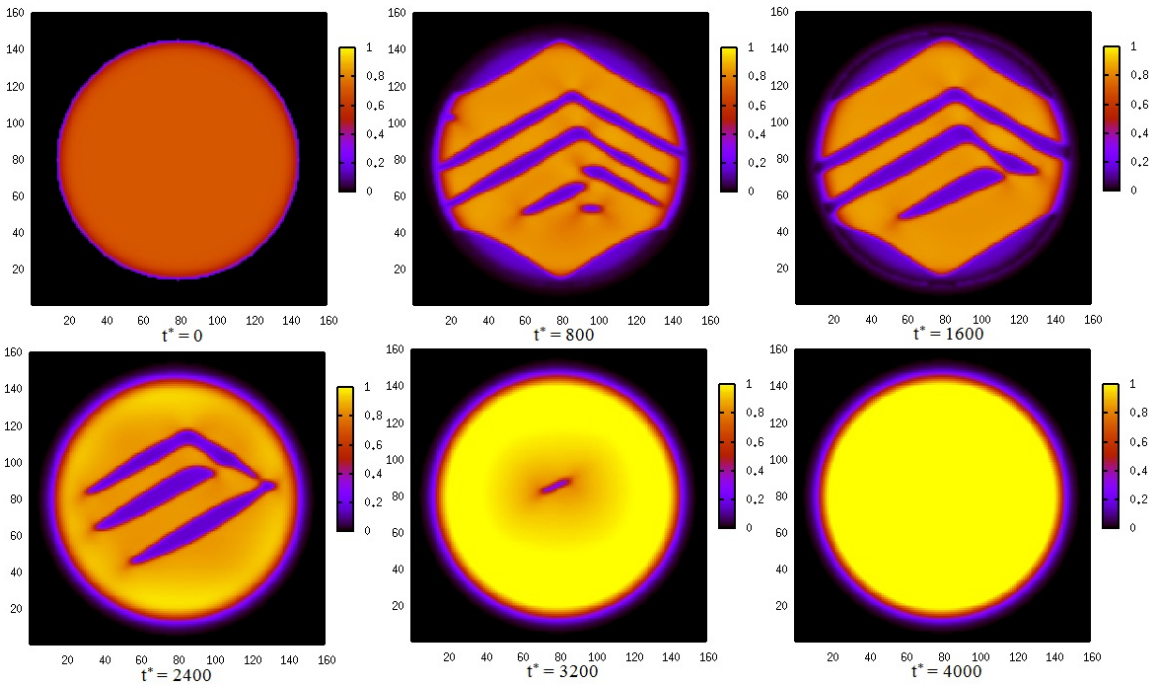

Fig. 5.11 Lithium concentration evolution with different time steps and isotropic mobility ($m_{xx} = 1, m_{yy} = 1$) at overpotential equal to 0.04 ($\eta = 0.04$) under fixed initial concentration ($C_0 = 0.7$) in a selected size nanoparticle in the Li-ion battery cathode.

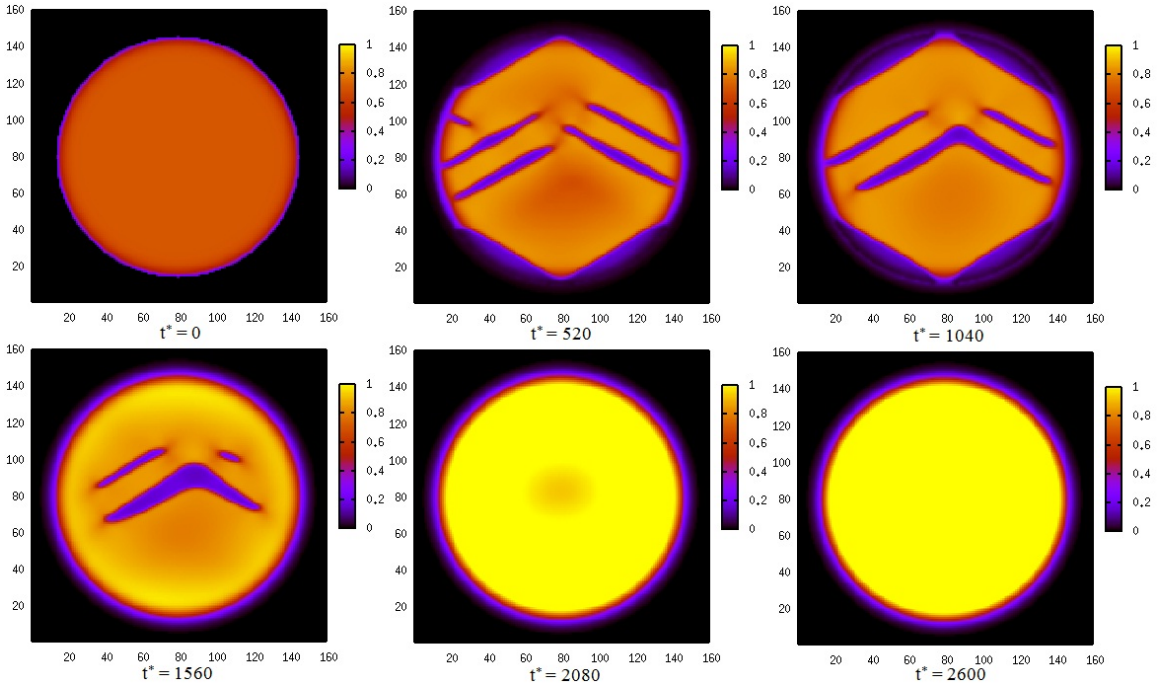

Fig. 5.12 Lithium concentration evolution with different time steps and isotropic mobility ($m_{xx} = 1, m_{yy} = 1$) at overpotential equal to 0.06 ($\eta = 0.06$) under fixed initial concentration ($C_0 = 0.7$) in a selected size nanoparticle in the Li-ion battery cathode.

5.5 Mobility effects on the morphology

Based on the experimental observations and first-principle calculations[3], the lithium inside the nanoparticle diffuses much faster along [010] direction. We designed a simulation to consider the effects of the anisotropy mobility along two dimensions on the microstructure of the particle. We compared the two cases, the isotropic and anisotropic mobility, while fixing the initial lithium concentration to $C_0 = 0.5$and overpotentialto $\eta = 0.02$. Figure 5.13 shows the isotropic mobility simulation case where the morphology of the microstructure is mainly determined by the spinodal decomposition,

lithium flux on the particle surface and misfit strain effects. The results are similar to previous cases.

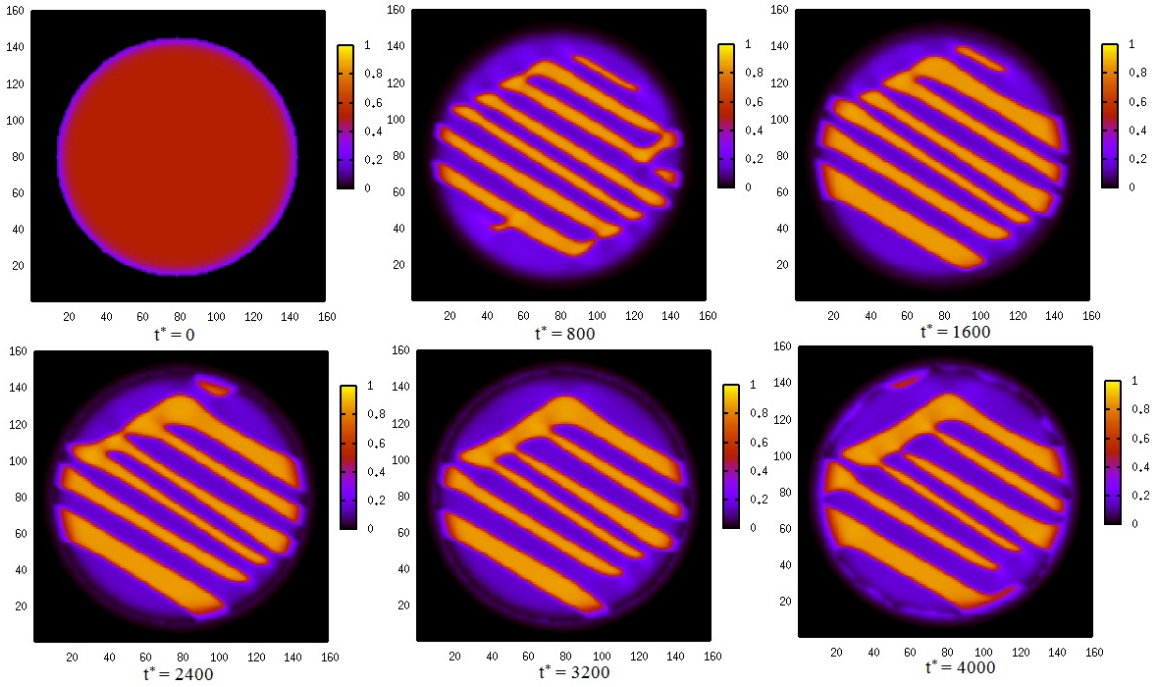

Fig. 5.13 Lithium concentration evolution with different time steps and isotropic mobility ($m_{xx} = 1, m_{yy} = 1$) under fixed overpotential ($\eta = 0.02$) and initial concentration ($C_0 = 0.5$) in a selected size nanoparticle in the Li-ion battery cathode.

In Fig. 5.14, we show the anisotropic mobility ($m_{xx} = 0.0001, m_{yy} = 1$) effects on the phase transition in the cathode with the fixed overpotential ($\eta = 0.02$) and initial concentration ($C_0 = 0.5$). The elastic energy causes the lithium concentration aligned along almost 45 degree to the horizontal line. However, the anisotropic mobility causes the lithium to diffuse much faster in y direction than in x direction. Both effects induce

the different morphology with the isotropic case, which illustrates that the lithium concentration is aligned along both directions.

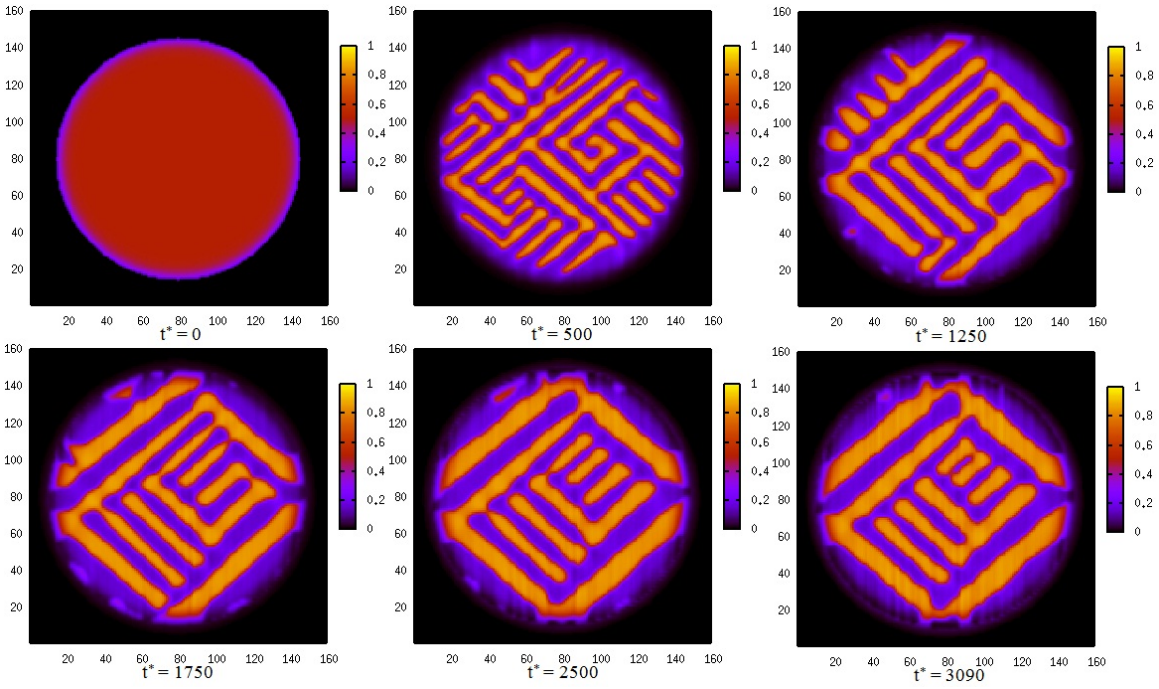

Fig. 5.14 Lithium concentration evolution with different time steps and anisotropic mobility ($m_{xx} = 0.0001, m_{yy} = 1$) under fixed overpotential ($\eta = 0.02$) and initial concentration ($C_0 = 0.5$) in a selected size nanoparticle in the Li-ion battery cathode.

5.6 Summary

In summary, we have developed a phase-field model to simulate and predict the lithium intercalation in the lithium-ion battery cathode. The effects of the initial lithium concentration, overpotential at the nanopaticle surface and diffusivity of lithium, and

elastic energy on the morphology of the microstructure and its evolution have been simulated. More detailed simulations such as lithium extraction from the particle, charging and discharging rate, and particle size effects need to be considered in further works.

References

[1] B. –O. Alfonso, P. –G. M.Víctor, and F. H.Flavio, *Private Communication*.

[2] B. –O. Alfonso andP. –G. M.Víctor,*Wiley InterScience*, **DOI10.1002**, 20103 (2005).

[3] S. Nashimura, G. Kobayashi, K.Ohoyama, R.Kanno, M.Yashima, and A. Yamada, *Nature Materials* **7**, 707-711 (2008).

[4] R. Amin, P. Balaya, and J. Maier, *Electrochemical and Solid-State Letters* **10**, A13-A16 (2007).

[5] R. Amin, J. Maier, P. Balaya, D. –P. Chen, C. –T. Lin, *Solid State Ionics* **179**, 1683-1687 (2008)

[6] R. A. Michael, V. Jens, S. U. Dirk, *Journal of Power Sources* **195**, 3922-3927 (2010)

CHAPTER 6

CONCLUSIONS AND FUTURE WORKS

6.1 Conclusion

In this thesis, the thermodynamics and two-phase morphologies of iron phosphate ($FePO_4$) and lithium iron phosphate ($LiFePO_4$) binary system has been studied by combining the phase-field method with microelasticity theory. Both the regular solution model and the modified regular solution model with a concentration dependent interaction parameter have been used to investigate the coherency strain energy contribution.

The optimum habit plane was shown in theoretically calculated phase diagram and three dimensional phase-field simulations. It was found that coherency strain energy could significantly suppress the miscibility gap. The modified regular solution model with a concentration dependent interaction parameter has been defined to match the experimental phase boundary data. With coherency energy contribution, the phase diagrams show a solid solution region around 0.3-0.7. This can explain why it has been proposed that solid solution phases exist at room temperature by Yamada et al. [1], which

is also consistent with the experimental phase boundary data. Theexcellent agreement between theoretical calculations and simulations indicate the optimum habit plane is preferred. However, the (100) habit plane (Fig. 3.7) [2] and (101) habit plane (Fig. 4.4) [3] have been observed in some experiments. Both (100) habit plane and (101) habit plane were observed in the experiments since they have extremely close total free energy. The possible reason the optimum habit plane was not observed in an experiment is due to defects which could partially lose coherency energy to show the minimum total energy, and also (100) may show lower interfacial energy than the optimum habit plane which gives the lowest total energy contribution.

The phase transitions and morphology of microstructure in a nanoparticle in the binary system due to the lithium diffusion process can be observed by combining the smooth boundary method and phase-field model. The concentration, overpotential and mobility effects have been observed and discussed in chapter 5.

6.2 Future Works

In chapter 5, we applied the phase-field model using smooth boundary methods on the regular solution model to investigate the morphologies of concentration, overpotential and mobility effects. However, it is desirable to apply this model on the modified regular solution model with a concentration dependent interaction parameter, since it shows excellent agreement with experimental observations.

The concentration effects will be different at temperature ranges which include: complete solid solution range, one small two-phase range, two two-phase range, and

large two –phase range. Several published papers [5, 6] have shown particle size effects in iron phosphate ($FePO_4$) and lithium iron phosphate ($LiFePO_4$) binary system. With this model, we can also be able to see the morphology of microstructure by the size changing. A modified phase-field model with a more complete description of applied voltage can be able to show more effects in the $FePO_4$-$LiFePO_4$ binary system.

References

[1] A. Yamada, H. Koizumi, N. Sonoyama, and R. Kanno, *Electrochemical and Solid-State Letters* **8**, A409 (2005).

[2] G. Chen, X. Song, T. J. Richardson, *Electrochemical and Solid-State Letters* **10**, A134-A138 (2007)

[3] C. V. Ramana, Z. Mauger, F. Gendron, C. M. Julien, K. Zaghib, Journal of Power Sources **187**, 555-564 (2009)

[4] A. K. Padhi, K. S. Nanjundaswamy, and J. B. Goodenough, *Journal of The Electrochemical Society* **144**, 1188 (1997).

[5] N. Meethong, H. –Y. S. Huang, C. W. Carter, and Y. –M. Chiang, *Electrochemical and Solid-State Letters* **10**, A134-A138 (2007).

[6] A. Yamada, H. Koizumi, S. –I. Nishimura, N. Sonoyama, R. Kanno, M. Yonemura, T. Nakamura, and Y. Kobayashi, *Nature Materials* **5**, 357-360 (2006).